

Reactive and Inelastic Scattering Dynamics of Hyperthermal O and O₂ from a Carbon Fiber Network

Savio J. Poovathingal,^{1,*} Min Qian,² Vanessa J. Murray,³ and Timothy K. Minton^{4,*}

¹*Department of Mechanical Engineering, 287 Ralph G. Anderson Building, Lexington, KY 40506, USA; saviopoovathingal@uky.edu; ORCID 0000-0001-7350-5104*

²*Department of Physics, School of Science, East China University of Science and Technology, Shanghai, 200237, China; mqian@ecust.edu.cn; ORCID 0000-0002-6472-7693*

³*Air Force Research Laboratory, Space Vehicles Directorate, 3550 Aberdeen Ave. SE, Kirtland AFB, NM 87117, USA; vanessa.j.murray@gmail.com*

⁴*Ann and H.J. Smead Department of Aerospace Engineering Sciences, 3775 Discovery Dr., University of Colorado Boulder, Boulder, CO 80303, USA; tminton@colorado.edu; ORCID 0000-0003-4577-7879*

Abstract

The reactive and inelastic scattering dynamics of ground-state atomic, O(³P), and molecular O₂(³Σ_g⁻) from a carbon fiber network at 1023-1823 K was investigated with a molecular beam-surface scattering technique. A molecular beam containing hyperthermal O and O₂ with a mole ratio of 0.92:0.08 and nominal velocity of 8 km s⁻¹ was directed at the network, and time-of-flight distributions of the scattered products were collected at various angles with the use of a rotatable mass spectrometer detector. O atoms exhibited both impulsive scattering (IS) and thermal

*Corresponding Author. Tel: 859 562-2854. E-mail: saviopoovathingal@uky.edu (Savio J. Poovathingal)

*Corresponding Author. Tel: 406 581-1080. E-mail: tminton@colorado.edu (Timothy K. Minton)

desorption (TD) dynamics, where the TD O-atom flux increased with surface temperature and the IS O-atom flux remained relatively constant. While the majority of the TD O atoms desorbed promptly after the beam pulse struck the network, signatures of thermal processes occurring over long residence times were also observed. Evidence of O₂ reactions was not observed, and the behavior of the inelastically scattered O₂ was invariant to the temperature of the network and showed both IS and TD dynamics. The dominant reactive product was CO, whereas CO₂ was a minor product. Both these products showed only TD dynamics. The observed flux of CO initially increased with temperature and then reached a plateau above which the flux no longer increased with temperature, over the temperature range studied. Thermally desorbed CO products exited the network promptly or after relatively long residence times, and two populations of CO with long residence times were distinguished. Hysteresis was observed in the temperature-dependent flux of thermally desorbed O and CO, with opposing trends for the two products. This work follows similar studies in our laboratory where the target materials were vitreous carbon and highly oriented pyrolytic graphite. The data suggest that the chemical reactivity of the three forms of *sp*² carbon surfaces is similar and that the differences arise from the variations of the morphology.

Keywords

Carbon oxidation, carbon ablation, carbon preform, gas-surface interactions, molecular beam scattering

1. Introduction

Space vehicles traveling at hypersonic speeds through a planetary atmosphere experience heat loads greater than 50 W cm^{-2} and require a heat shield to protect the vehicle from severe heating [1]. A class of materials used for several space missions consist of carbon-phenolic composites, where a network of carbon fibers is infused with a phenolic resin. Heat shields undergo a process called ablation (loss of material) under these extreme conditions. Ablation can occur through pyrolysis, gas-surface oxidation, and sublimation. Pyrolysis is the thermal decomposition of the phenolic resin, which occurs in the range of 200-1000 °C expelling the gaseous hydrocarbons out of the heat shield material [2,3]. Pyrolysis exposes the underlying carbon fiber network, which is a porous network of sp^2 carbon. Temperatures on the outer face of a heat shield can exceed 2000 °C under hypersonic entry conditions [4] and oxygen-containing atmospheric gases (e.g., O_2 , CO_2) may dissociate to oxygen atoms in the boundary layer, leading to aggressive oxidation of carbonaceous material. Ablative heat shields are currently overdesigned as a result of large uncertainties [1,4] in the understanding of the oxidation mechanisms. A better understanding of the oxidation process would enable improved carbon-oxygen kinetic rate models for computational fluid dynamics (CFD) [5–7] and direct simulation Monte Carlo (DSMC) simulations of heat shield behavior during hypersonic flight [8,9].

The oxidation of a porous carbon network (FiberForm) has been studied in flow-tube experiments where the reactive gas was O_2 [10–12]. Unlike in pure graphitic materials, O_2 diffuses easily into the porous network, causing in-depth oxidation under rarefied flow conditions because the reactivity of O_2 with carbon is low [10]. In contrast, such in-depth oxidation is unlikely to occur with a flow of atomic oxygen, because the high reactivity of O atoms will result in reactions before they have penetrated very deep [6]. Characterization of O_2 -oxidized fibers using SEM [13] showed

etch pits similar to those observed in the oxidation of HOPG [14]. Interest in graphene has prompted many experimental [15–19] and numerical [20–24] studies to examine the oxidation and reduction of HOPG and graphene oxide. Oxidation of HOPG by atomic oxygen has also been extensively studied to understand material degradation in low Earth orbit (LEO) [14,25,26]. Most experimental studies of the oxidation of HOPG by atomic oxygen have been limited to moderate surface temperatures (~ 1000 K or below), but a recent study from our lab reported O-atom reactive scattering dynamics on HOPG at temperatures up to 2300 K [19]. In addition, we have conducted similar experiments with vitreous carbon [27,28].

Key results that were obtained from the previous studies on our laboratory on the oxidation of hot HOPG and vitreous carbon were: (1) O_2 has extremely low reactivity compared with O atoms and scatters inelastically. (2) Even when incident O atoms have a very high translational energy of ~ 5 eV, they have a significant probability of sticking to the surface momentarily and then desorbing, and the probability of this process increases with surface temperature. (3) CO is the dominant reactive product and exhibits apparent non-Arrhenius behavior, with the flux of CO reaching a maximum and then decreasing as the surface temperature increases. (4) CO formation occurs mainly through reactions of adsorbed O, even when O atoms with very high incidence energies strike the carbon surface. (5) The probability of CO formation is dependent on the surface coverage of O. The apparent non-Arrhenius behavior of carbon oxidation has been observed in the past [29,30]. However, our work was able to explain this behavior as a competition between the thermal desorption of O and reaction to form CO [19,27,28].

In the work reported herein, we have extended the studies of HOPG and vitreous carbon to a porous carbon network in order to analyze the similarities and differences between the reactive and inelastic scattering dynamics of O atoms on flat, model sp^2 carbon surfaces and an sp^2 carbon

fiber network that is used in composite heat-shield materials. In addition to the potential differences in the oxidation reactions caused by the local carbon surface morphology, the scattering dynamics on a three-dimensional structure are expected to be much more strongly influenced by multiple-bounce scattering than the scattering dynamics on two-dimensional surfaces such as vitreous carbon and HOPG.

We have specifically focused our study on the carbon fiber network, FiberForm, which is the precursor network used in a material called phenolic impregnated carbon ablator (PICA). Recent NASA space missions, such as the Stardust sample return capsule [31] and Mars Science Laboratory (MSL) [32] have used PICA as the heat shield material [33,34]. A similar heat shield material, PICA-X, is used on Space-X's Dragon Capsule [35], and a PICA-type heat shield was used for the Hayabusa sample return mission of the Japanese Aerospace Exploration Agency (JAXA) [36]. The European Space Agency (ESA) has developed its own variant of PICA, known as ASTERM [37].

FiberForm consists of a three-dimensional network of rayon-based fibers with no surface treatment. During manufacturing, the fibers are pressed together and the plane where pressing is applied is referred to as the compression plane, or "in-plane." The fibers orient at an angle of $\pm 15^\circ$ relative to this plane [11]. The study of a carbon fiber network, like FiberForm, can reveal the extent to which conclusions from the oxidation of model systems can be useful to understand more complex engineering materials.

We have identified the main scattering channels when a molecular beam containing hyperthermal O and O₂ strikes a FiberForm network, and we have obtained translational energy distributions of scattered products as well as temperature- and angle-dependent distributions of product flux. The analysis of the new data with FiberForm revealed chemical processes for which

signatures were seen from vitreous carbon but were not analyzed in detail. Hence, in addition to analyzing the FiberForm results, we have also re-analyzed vitreous carbon data to facilitate in-depth comparison between the scattering dynamics of O and O₂ on FiberForm and vitreous carbon, both of which are expected to have local surface *sp*² carbon structures that are rough on an atomic scale.

2. Experimental Methods

The experiment employed a crossed molecular beams apparatus [39,40], which was reconfigured for studies of gas-surface interactions and has been described in detail previously [41,42]. A schematic diagram of the experimental setup can be seen elsewhere [27]. A brief description is provided here in the context of the current experiments.

A laser-detonation source [43] was used to produce hyperthermal beams containing argon (Ar beam) or a mixture of atomic and molecular oxygen (O/O₂ beam). For the both hyperthermal beams, a pulse of precursor gas (Ar or O₂) gas was produced by a custom piezoelectric pulsed valve, and this pulse entered a conical nozzle through a 1 mm orifice. The hyperthermal gas pulse was generated by the shock wave produced when a 7 J pulse⁻¹ CO₂ TEA laser was focused into throat of the nozzle and a high-temperature plasma was created. This pulsed hyperthermal source has been described previously [39] and was used with a repetition rate of 2 Hz. The O/O₂ beam was used for oxidation studies, and the Ar beam was used for where non-reactive incident molecules were desired to study only the effects of sample morphology on scattering dynamics. The hyperthermal beams passed through a skimmer, which had a diameter of 2 mm, and was further collimated by a 1.3 mm diameter aperture that was 3.5 cm from the skimmer. The total distance between the nozzle orifice and the sample surface (the center of rotation of the mass

spectrometer detector) was 99.2 cm, and the distance from the surface to the electron-impact ionizer of the detector was 34.4 cm. A synchronized chopper wheel, with three centrally-symmetric 1.5 mm width slots rotating at 300 Hz, was used to select a narrow velocity distribution from the overall beam pulse (before the beam pulse reached the surface). The O/O₂ beam had an average velocity of 7918 m s⁻¹ and a velocity width (full width at half maximum, fwhm) of 492 m s⁻¹. The beam was composed of O(³P) [44], with the balance being O₂(³Σ_g⁻) [45]. The average velocity of the Ar beam was 6223 m s⁻¹, with a fwhm of 318 m s⁻¹. Figure 2 shows the translational energies of O, O₂, and Ar in the O/O₂ and Ar beams, as well as the relative fluxes of O and O₂ in the O/O₂ beam. These quantities were derived from time-of-flight (TOF) distributions, obtained by directing the beams into the mass spectrometer detector and collecting mass-selected number density distributions as a function of time, $N(t)$, as the beam pulse passed through the detector ionizer.

The hyperthermal beams were directed at a FiberForm sample with an incidence angle of $\theta_i = 45^\circ$, and the products that scattered from the sample were detected by the rotatable mass spectrometer detector at various scattering (or final) angles, θ_f . Although the sample was a three-dimensional network of carbon fibers, the dimensions of the fibers and the spaces between them were far smaller than the overall sample dimensions, allowing a nominal surface to be defined. This surface is the macroscopic plane of the sample that faced outward toward the incident beam and the detector. In this paper, incidence and final angles are referenced to the normal to this nominal sample surface, where the incidence and final angles are on the opposite sides of the normal. The detector was rotated in the plane defined by the incidence angle and the surface normal. The products exiting the sample passed through the electron-impact ionizer [46] of the detector, located 34.4 cm from the nominal sample surface, and the ions produced were filtered

through a quadrupole and detected with a Daly-type ion detector [47] operating in a pulse-counting mode. Ion pulses were accumulated as a function of arrival time by a multichannel scaler, thus giving a time-of-flight (TOF) distribution of the products, which is proportional to number density as a function of time, $N(t)$. The TOF distributions were transformed into translational energy distributions, $P(E_T)$, where the area under a $P(E_T)$ curve is proportional to flux and can be integrated to obtain the total relative flux of the products that correspond to a given TOF distribution collected at a particular combination of θ_i and θ_f . Time zero in the TOF distributions is set by assuming a monoenergetic incident beam [48], with t_{zero} coming from the distance from the nozzle orifice to the sample surface (e.g., $t_{zero} = \frac{99.2 \text{ cm}}{7918 \text{ m s}^{-1}}$). The validity of the monoenergetic beam assumption for this analysis is discussed later. The raw TOF distributions were corrected for the ion flight time given by $\alpha \left(\frac{m}{z}\right)^{0.5}$ where m is the mass in amu, z is the charge, and α was determined empirically [48]. The TOF distributions of O were corrected for dissociative ionization of O₂ in the ionizer that came from the small O₂ component of the O/O₂ beam.

The FiberForm sample was provided by Fiber Materials, Inc. and was used as received (see Figure 1). The surface normal was parallel to the through-the-thickness (TTT) direction, which is perpendicular to the compression plane (described in Section I). A sample size of 28 mm × 8 mm × 1 mm was used, and the sample was heated resistively using a sample mount described previously [27]. Briefly, the sample mount was composed of two water-cooled copper electrodes that were electrically isolated by alumina spacers. The FiberForm sample, which has a resistance (at room temperature) of 2.3 Ohms along its long dimension, was clamped between the copper electrodes, and current was passed through the sample. The sample temperature was controlled by varying the current from 3.75 to 12.5 A. As the copper electrodes, to which the ends of the sample were clamped, were water-cooled, only the center of the sample reached a high temperature.

Nevertheless, the high-temperature region of the sample was significantly larger than the size of the molecular beam on the surface (1 mm high \times 1.7 mm wide). The sample surface temperature where it was struck by the molecular beam was measured with the use of a Leeds-Northrup optical pyrometer. Optical pyrometers are calibrated for surfaces with emissivity (ϵ) = 1 while the ϵ of carbon is \sim 0.8. The difference in computed flux using the observed temperature and estimated corrected temperature is small (see discussion in Supporting Information). Furthermore, the exact of emissivity of an oxidized FiberForm sample is unknown. Hence, we used the observed temperature in our analysis.

Two experimental data sets were collected for scattering with the hyperthermal O/O₂ beam. Before any data collection commenced, the sample was annealed in vacuum at 1823 K for at least one hour. In the first data set, TOF distributions of scattered products were collected over a surface temperature (T_s) range of 1023 K to 1823 K in 100 K steps. This study of the temperature dependence of the signal was performed with both increasing and decreasing temperatures. For the increasing temperature sweep, T_s was increased from 1123 K to 1823 K, and for the decreasing temperature sweep, T_s was decreased from 1823 K to 1023 K. For each temperature, TOF distributions were collected at fixed incidence and final angles of $\theta_i = \theta_f = 45^\circ$ for four products detected at mass-to-charge ratios of $m/z = 16$ (O⁺), 32 (O₂⁺), 28 (CO⁺), and 44 (CO₂⁺), with accumulation times corresponding to 500, 500, 1000, and 1000 beam pulses, respectively. The total data collection time at each temperature was 25 minutes. In the second data set, TOF distributions were collected at a variety of final angles in the range, $\theta_f = 5^\circ - 75^\circ$, with a fixed incidence angle of $\theta_i = 45^\circ$, at two surface temperatures, $T_s = 1023$ K and 1623 K. To account for any possible long-term drifts in the signal collected at various θ_f angles, the detection angle, θ_f , was incremented from low to high and then decremented from high to low, and TOF distributions

for all four products were collected at each θ_f . This procedure was repeated such that four TOF distributions corresponding to a particular m/z and θ_f were collected and were then added together. The total numbers of beam pulses corresponding to each TOF distribution collected for a given θ_f at $m/z = 16, 32, 28,$ and 44 were 2500 at $T_s = 1023$ K and 2000 at $T_s = 1623$ K, respectively. The translational energy distributions and mole fractions of O and O₂ in the O/O₂ beam used for the temperature sweep data set are shown in Figure 2, and the analogous data for the O/O₂ beam that was used for collecting the angular distributions of the scattered products are shown in Figure S1. The two beams had very similar energy distributions for O and O₂, but the mole fractions of O in the beams used for obtaining the two data sets were somewhat different: 92% for the first data set and 83% for the second data set. The same FiberForm sample was used for the collection of all the data with the O/O₂ beams.

For the experiments with the hyperthermal Ar beam, a pristine FiberForm sample was used to ensure that there would be no effect on the scattering dynamics of Ar from partially oxidized or etched carbon fibers. Again, the sample was annealed at 1823 K before data were collected. Analogous temperature sweep and angular distribution data were collected for Ar. The translational energy distribution of the hyperthermal Ar beam is shown in Figure 2; it had an average translational energy of 773 kJ mol⁻¹ and an energy width (fwhm) of 76 kJ mol⁻¹. For the temperature sweep data set, TOF distributions for $m/z = 40$ (Ar⁺) were collected for 250 beam pulses each over a sample temperature range of $T_s = 1023 - 1823$ K, with fixed incidence and final angles of $\theta_i = \theta_f = 45^\circ$. The total data collection time at each temperature was 2 minutes. The angular distributions were collected for $\theta_f = 5^\circ - 75^\circ$ at two sample temperatures of $T_s = 1023$ and 1623 K, with $\theta_i = 45^\circ$. The potential long-term drift was mitigated with one “round trip” by varying

θ_f from lowest to highest first, then from highest to lowest. The total numbers of beam pulses corresponding to each TOF distribution collected for a given θ_f at $m/z = 40$ was 500.

3. Results and Analysis

3.1. Scattering of Ar from FiberForm

TOF distributions of Ar atoms that scattered from FiberForm allowed us to analyze geometrical effects of the carbon fiber network on the scattering dynamics of particles that have no reactive interactions with the fibers. TOF distributions of scattered Ar corresponding to different sample temperatures and $\theta_i = \theta_f = 45^\circ$ are shown in Figure 3a. Bimodal TOF distributions such as these are commonly described in terms of two limiting cases [49–51], (1) non-thermal, impulsive scattering (IS), and (2) thermal desorption (TD). The IS component originates from atoms or molecules that undergo one or a few collisions on a surface before exiting to the gas phase with super-thermal velocities. Thus, IS products are characterized by early arrival times in a TOF distribution. In most cases, IS atoms or molecules retain some memory of the impinging collisions, and the dynamical behavior of the IS component typically depends on the incidence energy and angle [52–54]. The TD component originates from atoms or molecules that have a strong enough interaction with the surface to come into thermal equilibrium before desorbing with thermal velocities corresponding to a Maxwell-Boltzmann (MB) velocity distribution at the relevant surface temperature. TD products also typically exit a surface with an angular distribution of scattered flux that corresponds to $\cos\theta_f$. The deconvolution of the Ar scattering data into TD and IS components was accomplished by fitting the slow component of the TOF distribution with a MB distribution and then subtracting this distribution from the overall TOF distribution to obtain the IS distribution [27,41,48]. A MB distribution fit the slow components of the TOF distributions

remarkably well, as exemplified in the deconvoluted TOF distribution shown in Figure 3b. Translational energy distributions, $P(E_T)$, of the IS and TD Ar atoms were derived from the TOF distributions, and the integral of a given $P(E_T)$ distribution is proportional to total relative flux of the atoms that scatter at a particular θ_f . An example of the $P(E_T)$ distributions corresponding to IS and TD Ar atoms is shown in Figure 3d, and the integrated fluxes of the IS and TD Ar atoms as a function of sample temperature are shown in Figure 3c. In order to obtain the integrated fluxes of the IS component, the integration was restricted to a lower final energy ($\langle E_f \rangle$) limit of $2RT_s$, and the upper limit of $\langle E_f \rangle$ was restricted to the average energy of the incident Ar atoms, $\langle E_i \rangle$.

The presence of the TD component in the Ar TOF distributions (Figure 3b) is a consequence of the three-dimensional nature of the FiberForm “surface”. In previous studies of hyperthermal Ar scattering on planar surfaces of HOPG [19,26] and vitreous carbon [27] at elevated temperatures, only an IS component was present in the TOF distributions, suggesting that hyperthermal Ar atoms do not trap on high-temperature carbon surfaces long enough to come into thermal equilibrium before they exit to the vacuum. The presence of a TD component thus suggests that multiple bounces of Ar atoms in the porous three-dimensional carbon fiber network may cause loss of incidence energy and drive the atoms into thermal equilibrium before they eventually desorb from a carbon fiber and escape from the network. The fact that the TD components in the TOF distributions can consistently be fit well by a MB distribution at the surface temperature using t_{zero} as the time at which the incident beam pulse struck the sample is strong evidence that the Ar atoms do not diffuse out of the microstructure over long times. As will be discussed in more detail below, we refer to such TD behavior as “TD-prompt.” If the Ar atoms resided in the microstructure for more than ~ 100 microseconds (see Supporting Information), then there would be a slow tail in the TOF distributions that could not be fit by an MB distribution (“TD-slow”). This observation is

critical in analyzing the TOF distributions of scattered products following bombardment of FiberForm by O and O₂, which will be discussed below. Additional evidence for multiple-bounce scattering dynamics is seen in the representative IS $P(E_T)$ distribution shown in Figure 3d. The IS Ar atoms have a bimodal $P(E_T)$ distribution, with a higher-energy peak corresponding to final energies >100 kJ mol⁻¹ (IS-fast) and a lower-energy peak corresponding to final energies <100 kJ mol⁻¹ (IS-slow). Such bimodal translational energy distributions have been observed in several studies of hyperthermal atoms scattering from a surface [42,48,55,56]. The bimodal behavior could arise from backward scattering in the center-of-mass frame [42] or multiple bounces on a rough surface [48,57], although we prefer the latter explanation. Note that the $P(E_T)$ distribution shown in Figure 3d drops to zero before 600 kJ mol⁻¹ and we found that the probability of translational energies above the incidence energy of Ar ($\langle E_i \rangle = 773$ kJ mol⁻¹) was negligible for all combinations of incidence and final angles. This finding suggests that the monoenergetic beam approximation is valid for the analysis of the data presented here. Previous work in our laboratory has shown that the monoenergetic beam approximation breaks down if the $P(E_T)$ distribution extends well beyond $\langle E_i \rangle$ for the incident atom or molecule, in which case a forward convolution approach is required to fit the TOF distributions [48,55].

The angular distributions at two surface temperatures, $T_s = 1023$ K and 1623 K are shown in Figure S2 (Supporting Information). The IS angular distributions are fairly broad, as seen for atoms scattering from a liquid interface, which is rough on an atomic scale [48,56]. The TD-prompt angular distribution is fit well with a $\cos^n \theta_f$ distribution, with $n = 0.67$ at $T_s = 1023$ K and $n = 0.69$ at $T_s = 1623$ K. For thermal desorption of Ar atoms, which should have a relatively weak interaction with a carbon surface, n would be expected to be equal to 1. The reduced values of n for thermal desorption from carbon fibers in FiberForm may arise from the relationship between

the orientation of the fiber at the point of impact and the nominal surface normal that defines 0° in the experiment. Each fiber in FiberForm has a surface normal associated to it which may not be parallel to the nominal surface normal. Strictly speaking, an effective surface normal is parallel to the nominal surface normal only if the fibers are isotropic and randomly oriented. However, the manufacturing process causes the fibers to orient with the effective surface normal being $\pm 15^\circ$ relative to the nominal surface normal (see Introduction). As a result, the effective surface normal is not parallel to the nominal normal from which the experimental scattering angles are measured. The cosine distribution would appear rotated by angle α in the lab frame where α is the angle between the effective surface normal and the normal. Using the cosine-power fit, we can compute a range for the angle α by equating $\cos^{0.7}\theta_f = \cos(\theta_f - \alpha)$. The angle α lies between 1° and 7° , which is within the uncertainty of the FiberForm orientation. Thus, the cosine-power distribution of the thermal component for Ar scattering could be a result of the preferred orientation of the fibers. As will be discussed below, angular distributions of other thermally-desorbed species (O, O₂, and CO) also require a cosine-power fit. It is likely that the deviations from a pure cosine distribution are a result of the three-dimensional network of FiberForm.

3.2. Inelastic and Reactive Scattering of O and O₂ from FiberForm

TOF distributions of the four scattered products that leave the surface (O, O₂, CO, and CO₂) after it is struck by the incident O/O₂ beam pulse are shown in Figures 4a-d as a function of surface temperature. The TOF distributions of O exhibited IS and TD characteristics. The flux of the IS component stayed relatively constant across the range of surface temperatures investigated, while the TD component increased significantly with surface temperature. CO was the dominant reactive product, and CO₂ was a minor product, with very low signals observed above 1123 K.

The TOF distributions of O₂ contained IS and TD-prompt components that stayed relatively constant over the range of surface temperatures investigated. Qualitatively, the interactions of O/O₂ with FiberForm appear similar to those of vitreous carbon [27]. Hence, the findings of O/O₂ scattering from FiberForm are compared to vitreous carbon, and relevant TOF distributions of vitreous carbon have been re-analyzed in light of new insights from the FiberForm results.

The O₂ TOF distributions were decomposed into IS and TD-prompt components similar to the TOF distributions of scattered Ar. The flux of O₂ is shown in Figure 5c. The TD-prompt flux of O₂ is roughly equal to the IS flux, which is similar to the ratio of IS to TD flux for scattered Ar. The invariance of the TD-prompt component with respect to surface temperature indicates the absence of thermal mechanisms to form O₂ through surface recombination reactions. In the previous work on vitreous carbon, a slow-IS component of O₂ was observed at low temperatures which was attributed to Eley-Rideal (ER) reactions. Although a direct O-atom abstraction mechanism cannot be ruled out in FiberForm, the multi-bounce dynamics make it challenging to decipher possible ER reactions resulting in the formation of O₂. It is concluded that the O₂ signals arise from non-reactive scattering of O₂ from the surface based on the observations that the IS angular distributions of O₂ are analogous to IS distributions of O (Figure S2 Supporting Information), the similarities in the ratio of IS to TD-prompt flux for Ar and O₂ resulting from the three-dimensional porous geometry, and the invariance of flux with surface temperature. This result appears to disagree with a recent molecular beam-surface scattering experiment with a higher flux of lower-energy O atoms on vitreous carbon [28], where O-atom recombination to produce O₂ was reported to be significant. However, the recombination probability may depend strongly on the incident O-atom flux, which was 2-3 orders of magnitude higher in the recent experiment. In addition, the continuous beam of the recent experiment would be expected to

maintain a high surface oxygen coverage, which might also help to promote O-O recombination. Furthermore, it is not clear how sensitive the recombination probability is to the exact nature of the surface, which is presumably different between highly etched vitreous carbon and lightly etched carbon fibers in FiberForm.

In addition to the TD-prompt component that can be fit with a MB distribution, long (slow) tails were seen in the TOF distributions of O and CO (see Figures 6a and 6c) that could not be solely captured by a MB fit. With t_{zero} defined as the moment a beam pulse strikes the surface, a thermal event that roughly occurs over timescales greater than 112 μs (see Supporting Information for discussion) would appear slower in these TOF distributions. This was seen in vitreous carbon for CO [27], and an exponential decay fit was used to determine lifetimes of these slow processes. We extended this approach to obtain decay rate constants and flux components of processes occurring at long times. This method was suggested by Nathanson and co-workers to capture desorption events occurring over long times in molecular beam scattering from liquid surfaces [55].

Consider a CO desorption event of the following form: $\text{C}(\text{O}) + \text{C}_s \rightarrow \text{CO}$. In this chemical equation, $\text{C}(\text{O})$ corresponds to species that desorb to form CO and C_s is the participating group of surface atoms. Previous theoretical work has indicated that desorption events from isolated $\text{C}(\text{O})$ functional groups are unlikely because the barrier is too high, but the presence of adsorbed O lowers the energy barrier significantly [23]. Therefore, C_s in the chemical equation above refers to reactive sites on the carbon material and adsorbed O that participate in the reaction. Under the assumption of pseudo first-order kinetics, i.e., $[\text{C}_s] \gg [\text{C}(\text{O})]$, the rate of CO desorption would be proportional to $e^{-k[\text{C}_s]t}$, where t is the time and k is the rate constant. The slowly desorbing products exit the surface with thermal velocities; hence, the number density distribution of their

arrival times (TOF distribution) would be a convolution of the exit thermal velocity determined by the MB distribution and the desorption rate. Because it is difficult to infer $[C_s]$, we are effectively estimating the product of k and $[C_s]$ through the fits and we refer to the decay-rate constants obtained from the fits as k_{eff} which has the units of time^{-1} . Two slow processes were identified in the TOF distributions of CO and one slow process was identified in TOF distributions of O. To distinguish various thermal processes, the component that is fit solely with a MB distribution is referred to as TD-prompt; the slow process observed for O is referred to as TD-slow; and the two slow processes observed for CO are referred to as TD-slow1 and TD-slow2 respectively.

The TOF distributions of O are fit as follows. The analytical MB distribution is fit first to obtain the TD-prompt component. The signal at long times (TD-slow) is fit by varying k_{eff} , and the IS component is obtained by subtracting the total TD signal from the total TOF distribution, while restricting the integration of the IS component to a minimum final energy of $2RT_s$ J mol⁻¹. As described earlier, the flux components are obtained by transforming the TOF distributions into translational energy distributions, $P(E_T)$, and integrating the respective areas. As signals at long times (TD-slow) were observed for scattered O from FiberForm, the TOF distributions of scattered O from vitreous carbon were carefully re-examined. However, we could not find signatures of TD-slow in the scattering of O from vitreous carbon. Representative TOF distributions of O are shown in Figures 6a and 6b for FiberForm and vitreous carbon respectively. There is an effusive background in the O and O₂ signals that originates from the source [19,27], which restricts our analysis of TOF distributions to flight times below 1200 μs . Although our analysis for O is restricted to 1200 μs , a definite signal for TD-slow can be seen in FiberForm but not in vitreous carbon. The TD-slow signal decreases as the surface temperature is increased, with the TD-slow flux accounting for ~8% of the total flux at 1123 K and ~5% at 1823 K. The flux components of

O are shown in Figures 5a and 7a for FiberForm and vitreous carbon respectively, for both the increasing and the decreasing temperature surveys. The TD-prompt flux increases markedly beyond 1200 K for vitreous carbon which may be ascribed to surface-adsorbed O desorbing promptly as the surface temperature is increased [5,27,28]. A similar trend is observed for FiberForm, where the TD-prompt flux dominates beyond 1300 K. However, the rate of TD-prompt flux increase for vitreous carbon is approximately 2.8 times faster than for FiberForm. There is a marginal increase in TD-slow flux with surface temperature, but it is difficult to discern trends, because the variation over the wide range of surface temperatures is small. The angular distributions of O at $T_s = 1023$ K and 1623 K for FiberForm are shown in Figure S2 (Supporting Information). The TD-prompt fluxes can be fit well with a cosine-power distribution, $\cos^n \theta_f$, with $n = 1.27$ at $T_s = 1023$ K and $n = 1.56$ at $T_s = 1623$ K. The angular distribution of the IS flux for FiberForm is much broader than for vitreous carbon, as would be expected for a rough surface. Finally, the thermal fluxes are higher in the decreasing temperature survey when compared to the increasing temperature survey. This is a manifestation of a hysteresis effect that is discussed below.

The CO signals from FiberForm exhibited only TD characteristics. As described earlier, three processes were identified and are referred to as TD-prompt, TD-slow1, and TD-slow2. TD-slow1 and TD-slow2 are distinguished by the order of magnitude of the desorption rates. The effective decay rate of TD-slow1 is around $10^{-3} \mu\text{s}^{-1}$ (lifetime $\sim 10,00 \mu\text{s}$) and the decay rate of TD-slow2 is around $10^{-5} \mu\text{s}^{-1}$ (lifetime $\sim 100,000 \mu\text{s}$). In the previous work on vitreous carbon [27], one slow CO process with a lifetime of $1500 \mu\text{s}$ was identified at 800 K. After re-examining the TOF distributions of CO from vitreous carbon, we have identified two slow processes (TD-slow1 and TD-slow2), akin to those observed in FiberForm. TOF distributions of CO for FiberForm and vitreous carbon are shown in Figures 6c and 6d respectively. We have also quantified the flux of

TD-slow1 and TD-slow2 from vitreous carbon in a similar manner described above. Unlike O, CO TOF distributions do not contain an effusive background, enabling us to analyze TOF distributions for the duration of the pass length in the experiment, which was 20,000 μ s.

A conventional deconvolution of the TOF distributions is not possible when slow processes are considered, because there is considerable overlap between the thermal signals (TD-prompt, TD-slow1, and TD-slow2). We used two methods to fit the TOF distributions: (1) residual fit and (2) simultaneous fit to obtain the upper and lower bounds for the thermal components of CO flux. In the residual fit, TD-prompt is fit first to capture most of the signal, TD-slow1 is fit next followed by TD-slow2 (Figure 6c). In the simultaneous fit, both TD-prompt and TD-slow1 are adjusted simultaneously to capture the TOF distributions, and the remaining portion is fit with TD-slow2 (see Figure S3a, Supporting Information). The residual fitting method provides an upper bound to the flux of TD-prompt and a lower bound to the flux of TD-slow1, while the simultaneous fitting method provides a lower bound to TD-prompt and an upper bound to TD-slow1. We found that the residual fitting process was more robust, as the activation energies obtained from the simultaneous fit were inconsistent with the expected trends. Attempts to perform the residual fitting method in reverse – i.e., fit the slow signal first and then fit the remaining signal with a MB distribution did not capture the rising portion of the TOF distribution and always resulted in an underprediction of the total flux. After the fitting of the TD component of a TOF distribution was complete, the IS component was obtained by subtracting the total thermal component (TD-prompt+TD-slow1+TD-slow2) from the total TOF distribution. The IS component in the TOF distributions of FiberForm was negligible; however, a non-negligible IS component (~10-15 %) was seen for vitreous carbon. Previous analysis suggested that this signal arose from a complicated thermal process on the surface or uncertainties in the surface temperature measurement [27]. The

angular distribution of the IS component in vitreous carbon appears to have thermal characteristics with a cosine-power distribution; therefore, the IS flux from vitreous carbon was added to the TD-prompt flux.

The fluxes of CO obtained using the residual fitting method are shown in Figures 5b and 7b for FiberForm and vitreous carbon respectively. The TD-prompt flux of CO reaches a maximum at 1400 K and then decreases for vitreous carbon, while it plateaus at 1723 K for FiberForm. The flux of TD-slow1 and TD-slow2 become vanishingly small at temperatures greater than 1700 K for vitreous carbon, but these signals persist in FiberForm. However, the TD-slow1 flux of FiberForm reaches a maximum at 1400 K and then decreases as the surface temperature is increased. Previous analysis of vitreous carbon data has indicated that CO formation depends on the coverage of O on the surface. As the surface temperature is increased, the surface loses O-atom coverage through desorption of O, limiting CO production. The increased surface area of FiberForm would allow a higher steady-state oxygen coverage as compared to vitreous carbon, as desorbing atoms can re-adsorb on a different fiber. Higher O-atom coverage would shift the temperature at which CO peaks to higher values because more reagents are available on the surface for CO formation. Thus, the plateau observed in the TD-prompt flux from FiberForm at a surface temperature higher than from vitreous carbon is consistent with a surface-coverage-dependent mechanism for CO desorption. The coverage-dependent mechanism for CO desorption is also consistent with the peak observed in the flux of TD-slow1 at 1400 K for FiberForm. The angular distributions of CO at $T_s = 1023$ K and 1623 K for FiberForm are shown in Figure S2 (Supporting Information). The TD-prompt and TD-slow1 fluxes can be fit well with a cosine-power distribution, $\cos^n \theta_f$, with $n = 1.16$ and $n = 1.02$ for TD-prompt and TD-slow1, respectively, at $T_s =$

1023 K, and with $n = 1.07$ and $n = 0.6$ for TD-prompt and TD-slow1, respectively, at $T_s = 1623$ K. The TD-slow2 fluxes were too small to discern a definite cosine-power distribution.

The effective rates obtained from the residual fits of TD-slow1 and TD-slow2 were used to compute apparent activation energies using an Arrhenius law, $k = Ae^{-E/kT}$. The energies obtained through these fits should not be considered as barriers for elementary processes. These are effective barriers arising from the competition of various processes occurring on the FiberForm surface. The Arrhenius fits for FiberForm and vitreous carbon are shown in Figures 7c and 7d respectively. The energies obtained for FiberForm are 32.2 kJ mol^{-1} and 59.6 kJ mol^{-1} for TD-slow1 and TD-slow2 respectively, while the energies predicted for vitreous carbon are much lower (TD-slow1 = $11.11 \text{ kJ mol}^{-1}$ and TD-slow2 = $19.42 \text{ kJ mol}^{-1}$). The effective rate constants in our fits contain two terms, k and $[C_s]$, where $[C_s]$ depends on surface coverage. As FiberForm is expected to have a higher coverage of O, $[C_s]$ would be higher in the case of FiberForm. Therefore, the estimated energies from the fits are consistent with the expected trends. Inconsistencies were observed when the simultaneous fitting method was used to analyze the TOF distributions. The TD-prompt component of the CO flux continues to increase exponentially even at the highest temperatures (Figure S3b, Supporting Information) with this fitting procedure. Furthermore, the Arrhenius activation energy is higher for the faster decay process (TD-slow1), which is unrealistic (Figure S3c, Supporting Information). Analysis of TOF distributions of CO from vitreous carbon exhibited the same trends for the simultaneous fitting method. These two observations suggest that the residual fitting method is a more robust approach to fit the TOF distributions. Although the activation energies are different, the relative fluxes of thermal CO (TD-prompt, TD-slow1, TD-slow2) show similar trends in both FiberForm and vitreous carbon. This can be seen in Figure 8a, where the flux percentages of the thermal components of CO are plotted. The similarities in TOF

distributions and fluxes at various surface temperatures suggest that the chemical reactivities of FiberForm and vitreous carbon are similar.

The flux of CO exhibits a temperature-dependent hysteresis, as seen in Figure 5b. Such a hysteresis has been observed in the past by Olander et al. on the oxidation of pyrolytic graphite by O₂ [58], and it was also observed in our previous work on vitreous carbon [27,28]. Comparing the TD-prompt fluxes of CO and O, we see that the TD-prompt flux of O has an opposite trend compared to TD-prompt CO. This holds true for FiberForm (Figures 5a and 5b) and vitreous carbon (Figures 7a and 7b). Hysteresis arises because the surface takes a long time to reach a steady coverage and 25 minutes at each surface temperature is insufficient to reach steady coverage. To analyze the effect of hysteresis, we compute the flux difference, ($CO_{increase} - CO_{decrease}$) which is shown in Figure 8b for FiberForm and vitreous carbon. At high surface temperatures, the surface oxygen coverage would be expected to reach a minimum under steady-state conditions. A higher difference would imply that the surface has lower coverage of O and is closer to steady-state conditions. As seen in Figure 8b, the difference is higher for vitreous carbon, consistent with our hypothesis that vitreous carbon has a lower coverage of O atoms. The difference in the total thermal flux of O between the two temperature curves is also shown in Figure 8b. A quantitative comparison cannot be performed because the fluxes have not been corrected for the mass-dependent detection sensitivity of our detector. However, qualitatively, the flux difference of O exhibits the opposite trend compared to CO.

CO₂ was a minor product in the reactions with both FiberForm and vitreous carbon (Figures 4d and 5d). However, CO₂ signal persists to a higher temperature in FiberForm (Figure 4d) compared to vitreous carbon, and two TD-slow processes, as with CO, were required to fit the CO₂ TOF distributions from FiberForm, unlike the TOF distributions from vitreous carbon which

returned to zero and required only a prompt thermal (MB) fit [27]. As the signals were very low above 1023 K, the reactive dynamics of CO₂ are not discussed in this article.

4. Discussion

The TD-prompt component in the TOF distributions of Ar atoms that scatter from FiberForm arises from the three-dimensional network of carbon fibers, which presumably causes multiple bounces of the incoming atoms on different surfaces of the individual carbon fibers and drives them toward thermal equilibrium through inelastic energy transfer on each bounce. Such thermal scattering dynamics was not observed in our earlier similar studies of hyperthermal Ar atoms scattering on the two-dimensional surfaces of vitreous carbon [27] and HOPG [59], where we observed only non-thermal scattering with angular distributions that were lobular and peaked far away from the surface normal. The lobular angular distribution of scattered Ar from vitreous carbon was slightly broader than that from HOPG. An individual fiber that is rougher, on an atomic scale, than the surface of vitreous carbon would be expected to promote randomization of the scattering angle distribution and result in a localized angular distribution that is relatively broad, but it would not lead to a significant TD-prompt component following impact by highly energetic incident Ar atoms. Studies of Ar scattering from liquid hydrocarbons [57] (squalane and PFPE), which are very rough on an atomic scale, showed that the TD-prompt fraction in the TOF distributions was only ~30%. In contrast, the percentage of TD-prompt Ar flux was ~50% from FiberForm, indicating that the TD-prompt component arises from multiple bounces of Ar and not from the roughness of individual fibers.

The deconvolution of the TOF distributions of scattered Ar into IS and TD-prompt components is evidence that Ar is not trapped within the FiberForm microstructure for long times. Similarly, the TOF distributions of non-reactive O₂ can be decomposed purely into IS and TD-

prompt components. As there are no Ar or O₂ signals that persist long enough to suggest residence times beyond ~100 microseconds (the resolution of our experiment), we conclude that the signals that give rise to the long tails of the TOF distributions for O and CO are not simply the result of trapping within the three-dimensional porous network of FiberForm.

Recent work on the oxidation of HOPG by Murray et al. indicates barriers to the desorption of CO and O that increase with decreasing surface oxygen coverage [19]. The desorption barrier shifts the TOF distributions to shorter times than predicted by a MB distribution at the surface temperature. In contrast, TD TOF distributions obtained from FiberForm and vitreous carbon were fit well under the assumption of a MB distribution for the thermal desorption processes, suggesting little or no barrier to desorption. It is likely that oxygen surface coverage on FiberForm, and perhaps on vitreous carbon, would be much higher than on HOPG, resulting in lower energy barriers for CO desorption. On FiberForm, the likelihood for O atoms to chemisorb on the surfaces of individual fibers is high as a result of the potential for many bounces in the fiber network. In addition, the carbon surfaces on FiberForm and vitreous carbon presumably have myriad defects that would lead to increased sticking of O atoms on these surfaces compared to the much more ordered surface of HOPG. Indeed, the reactivity of HOPG is significantly lower than that of vitreous carbon or FiberForm, as indicated by the relatively low signals of CO from HOPG and the small fraction of TD O atoms. Thus, surface oxygen coverage must be playing a significant role in the fate of oxygen atoms that bombard the different types of *sp*² carbon surfaces. The higher oxygen coverage on FiberForm and vitreous carbon opens many pathways for CO desorption following relatively long surface residence times, such as those that we have observed.

Signals at long times were observed in the TOF distributions of O atoms that desorbed from FiberForm but not from vitreous carbon. Unlike scattering of inert gas atoms, such as Ar, O

atoms can chemisorb on a carbon surface and those that desorb from one fiber in FiberForm can re-adsorb on a different fiber with a finite residence time. The aggregation of adsorption residence times on different fibers caused by multiple bounces could result in a TD-slow signal in the TOF distributions of O atoms that desorb from FiberForm. Although a new chemical pathway for desorption of O cannot be ruled out, the absence of TD-slow signatures in O desorbing from vitreous carbon in light of the otherwise similar reactive scattering dynamics on FiberForm and vitreous carbon suggests that the TD-slow signal for O desorbing from FiberForm is likely a result of multiple bounces and adsorption events within the three-dimensional porous network of FiberForm.

Signals at long times persist in the TOF distributions of CO reactive products for both FiberForm and vitreous carbon. The work of Marchon et al. indicates that the probability of CO adsorption on a carbon surface is very low [60]. Hence, TD-slow1 and TD-slow2 cannot be attributed to the three-dimensional network of FiberForm alone. In the previous work on vitreous carbon [27], it was suggested that the slow signals of CO observed at 800 K might be attributable to the Boudouard reaction, where CO_2 reacts with the carbon surface to form CO. Typical activation energies reported in the literature [61–63] for Boudouard reactions are greater than 100 kJ mol^{-1} . Although the mechanism for a Boudouard reaction is not well understood, the rate-limiting step typically involves the abstraction of adsorbed O by CO_2 from the surface [64,65]. The experiments reported in the literature [66–68] examined the reaction close to atmospheric conditions while our experiments are performed under vacuum. The carbon surface has a much lower O-atom coverage in our experiments; hence, we would predict a much higher activation energy for the Boudouard reaction. However, the activation energy we obtained from our fits is around 40 kJ mol^{-1} (TD-slow1 in Fig. 7c). The maximum possible activation energy from the data

can be estimated by using the rate from the residual fit method at 1023 K and the simultaneous fit method at 1823 K. The maximum activation energy estimated from our experiments is 65 kJ mol^{-1} , which is considerably lower than those reported in the literature. Furthermore, FiberForm would have a higher oxygen coverage compared to vitreous carbon and the Boudouard reaction would thus be favored in FiberForm. In contradiction to the expected higher reactivity and thus depletion rate of CO_2 on FiberForm vs. vitreous carbon, the observed CO_2 signals persists at higher sample temperatures for FiberForm than for vitreous carbon. Finally, we see two distinct slow processes (TD-slow1 and TD-slow2) in TOF distributions of CO and it is improbable that the same reaction would exhibit two different rate constants. Thus, we conclude that it is unlikely that the TD-slow1 and TD-slow2 signals in the CO TOF distributions, either from FiberForm or vitreous carbon, originate from a Boudouard reaction.

Comparison of our results to other experimental and theoretical studies suggest that the CO desorption rates observed are a consequence of different carbon-oxygen functional groups that are formed after O chemisorbs on the surface. Tremblay et al. [66] showed the presence of at least two functional groups on a carbon surface and further studies have shown the presence of multiple functional groups on the surface. Typical functional groups attributed to the formation of CO are ethers, semi-quinones, lactones, anhydrides, and furan/pyrone structures [16,67–69]. A few representative functional groups that are formed on a carbon surface are shown in Figure S4 (Supporting Information). Although there is consensus on the broad nature of functional groups, there is disagreement on the exact functional groups being formed on the surface. The DFT results of Sun et al. [23] and Carlsson et al. [70] indicate that the energy barriers of CO desorption from isolated ethers and semi-quinones are greater than 1 eV. However, the presence of O adsorbed on neighboring carbon sites lowers the energy barrier significantly. The simulation results suggest

that CO desorption occurs from lactone-type structures where a lactone group is surrounded by a neighboring ether structure. On a complicated surface like FiberForm, the desorption of CO can create new structures that can be further sites for CO desorption. For example, the desorption of CO from an ether-lactone-ether structure would result in a lactone-ether structure which is another reactive site for CO desorption [23]. Thus, the CO desorption rates observed in our experiments may arise from different combinations of lactone and ether groups that are formed on the surface. Many experiments [18,66–68] have been performed on different carbon materials with O₂ as the reacting gas, and adsorption of O₂ was performed at low surface temperatures. Similarly, the DFT [23,69] and MD simulations [16] were limited to studies on single-layer graphene. On a complex surface, additional groups could be formed. For example, MD simulations of Bagri et al. indicate the formation of 5-membered carbon rings, quinones in 1-2, 1-4 configurations [69]. Sun et al. found that energetically degenerate structures of ether-lactone pairs can lead to CO or CO₂ formation depending on the relative position of the ether group with respect to the oxo termination of the lactone group. Thus, even on an idealized graphene sheet, the CO desorption process is quite complex, with several possibilities arising from the configuration of adsorbed O atoms. Furthermore, it is quite likely that these carbon-oxygen functional groups can form from intercalated oxygen atoms, as has been suggested by Paci and Paci [71]. They found that the desorption of reaction products from below the surface would require the surmounting of multiple barriers, which would be consistent with a longer apparent residence time of oxygen on (or in) the surface. Chemisorption of intercalated N atoms has also been observed in a recent theoretical study by Guo and coworkers on the interaction of N atoms with a layered graphene surface [72]. The absorption of oxygen into the carbon bulk and slow release of reactive and non-reactive products has been hypothesized to explain the temperature-dependent total flux of O-containing products

in experiments on O atoms interacting with vitreous carbon. The complexity of the fiber surfaces of FiberForm and the numerous possibilities of O-atom adsorption, absorption, and desorption prevent us from assigning the three identified TD rates to distinct mechanisms. We can only speculate here that TD-slow1 and TD-slow2 might involve slow reactions occurring in the bulk. This speculation is supported by the observation that these very slow processes disappear at high sample temperatures, leaving only TD-prompt products. At high temperatures, the prompt desorption of surface-bound O and CO products into the vacuum would be expected to compete more effectively with diffusion of O into the bulk.

A temperature-dependent hysteresis is observed in the product O and CO flux from both FiberForm and vitreous carbon (Figures 5a, b, and 7a, b) and cannot be attributed to the microstructure of FiberForm. The previous work in our laboratory on vitreous carbon, conducted with a hyperthermal O/O₂ beam in a similar fashion as the experiments with FiberForm described here, showed that it could take more than three hours for the surface coverage to reach steady state on vitreous carbon at 1875 K [27]. In the temperature survey study, the product fluxes were collected for approximately 25 minutes at each surface temperature. As a result, the surface coverage did not reach steady state during data collection at each surface temperature, and the surface coverage was thus constantly decreasing. The surface coverage was much lower after the sample temperature had been raised to 1875 K and then was decreasing, resulting in a lower flux of desorbed CO. A similar temperature-dependent hysteresis was first reported by Olander et al. [58], who observed it in the CO products of experiments with O₂ scattering on pyrolytic graphite. They suggested a thermal annealing mechanism that removed reaction sites from the surface at high temperatures. According to the hypothesis of Olander et al., as the temperature is reduced from a high value to a low value, the reaction sites were not regenerated fast enough, resulting in

hysteresis. The scattering results with Ar suggest that thermal roughening had no impact on the scattering or reactive behavior [27], and it is not clear how the thermal annealing mechanism would be activated as the temperature is increased. Signatures of hysteresis were also seen in certain TPD results [68,74,75], although the authors did not use this terminology.

A similar temperature-dependent hysteresis in O and CO product flux has also been observed in our earlier studies of the oxidation of vitreous carbon [27,28], and it has been discussed in detail in the context of the more recent study that employed a continuous and high-flux beam of oxygen atoms [28]. The basic explanation is likely the same for the oxidation of FiberForm. The temperature-dependent hysteresis may arise from the intercalation of oxygen atoms between graphitic planes, which desorb as O, O₂, or CO at high temperatures on the time scale of minutes to hours. The energy-barrier dependence of CO formation on oxygen coverage could also play a role. Consider a carbon material (FiberForm or vitreous carbon) initially at a high surface coverage. At high surface temperatures, CO and O desorb, thus lowering the surface oxygen coverage, but as the coverage reduces, the barrier to form CO increases [19,23]. Once the energy barriers are greater than the available thermal energy, the desorption process shuts down and the surface reaches a quasi-steady transient coverage that depends on the supply of O atoms from the incident beam. In the experiments with the pulsed hyperthermal O/O₂ beam, when a subsequent beam pulse arrives at the sample, a new dose of O atoms on the surface lowers the energy barriers, resulting in further CO desorption until a new quasi-steady transient state is achieved. This is a continual process where the incoming beam pulse aids in removing a subset of functional groups, and this continuous process occurs until the surface reaches a steady state over the course of minutes to hours. As has been discussed previously [28], a high flux of O atoms, especially from a continuous rather than a pulsed source, reduces hysteresis and the maintenance of a high surface coverage at

all times would be expected to result in the same temperature-dependent reactivity regardless of whether the temperature is increasing or decreasing.

5. Conclusions

The reactive and non-reactive scattering dynamics of hyperthermal O and O₂ on a carbon fiber network (FiberForm) at high surface temperatures were investigated using a molecular beam-surface scattering technique. Four scattered products (O, O₂, CO, and CO₂) were observed, and the translational energy distributions of the scattered products were collected for various surface temperatures and scattering angles. The dominant non-reactive product was O and the dominant reactive product was CO. The O₂ present in the beam scattered non-reactively and no signature of surface recombination of O atoms was found in the O₂ scattering data, most likely because of the low flux of incident O atoms in the incident beam. CO₂ was a minor reaction product, with very low signals above a sample temperature above ~1100 K. The signals of O contained both impulsive scattering and thermal desorption characteristics, with the thermal desorption component increasing significantly with sample temperature. The dominant reactive product, CO, exited the surface only through thermal desorption mechanisms. The CO signals contained a prompt thermal component and two populations of slow, thermal CO with long desorption times following the incident O/O₂ pulse, giving an apparent residence time on the surface. The residence times for the slow processes were around 1000 μs and 100,000 μs and the relative proportions of the slow processes decreased with surface temperature. In addition to prompt thermal fluxes, the fluxes of the slow processes were quantified, and the apparent activation energies were inferred for the two slow processes. Slow thermal processes were also observed in the signals of O, but the relative proportions compared to prompt thermal desorption were much smaller for O vs. CO. The flux of

O and CO exhibited opposite trends in a temperature-dependent hysteresis, indicating a competition between thermal desorption of O and CO and suggesting the possible presence of absorbed oxygen that could slowly be released from the bulk. The data obtained from an earlier analogous study on vitreous carbon were re-analyzed in light of new insights from the FiberForm experiment and compared to the results of this experiment.

The results from the analysis of the data on the oxidation of FiberForm and vitreous carbon indicate that the chemical processes occurring on both carbon surfaces are similar. The differences in the reactive and non-reactive scattering dynamics could be attributed to the higher oxygen coverage on the carbon fibers of FiberForm, afforded by the microstructure of FiberForm which promote multiple-bounce scattering and a concomitant increase in the sticking probability. A companion experiment on the inelastic scattering of Ar demonstrated the multi-bounce dynamics on FiberForm that were absent in the scattering from vitreous carbon. The study described here strongly suggests that the differences observed in the interactions of oxygen atoms with hot FiberForm and vitreous carbon are a result of the qualitatively different morphology of the two sp^2 carbon materials and not significant differences in their chemical reactivity.

Acknowledgements

This work was supported by NASA (Grant Nos. NNX15AD77G and 80NSSC18M0065). The experimental data were collected and much of the analysis was completed when all the authors were affiliated with Montana State University Bozeman. The authors would like to acknowledge Prof. Kelly A. Stephani and Dr. Krishnan Swaminathan-Gopalan for insightful discussions.

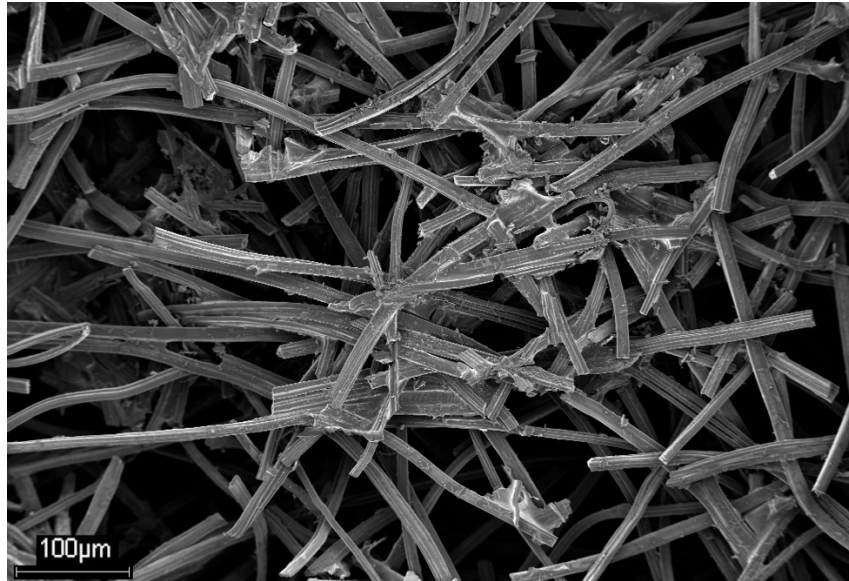


Figure 1. Scanning Electron Microscope (SEM) image of FiberForm, viewed normal to the sample (pressing) plane, that was exposed to the O/O₂ beam.

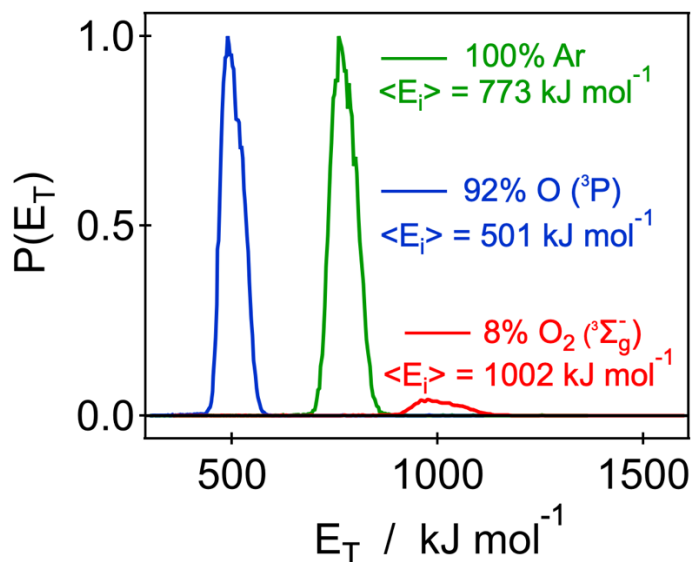
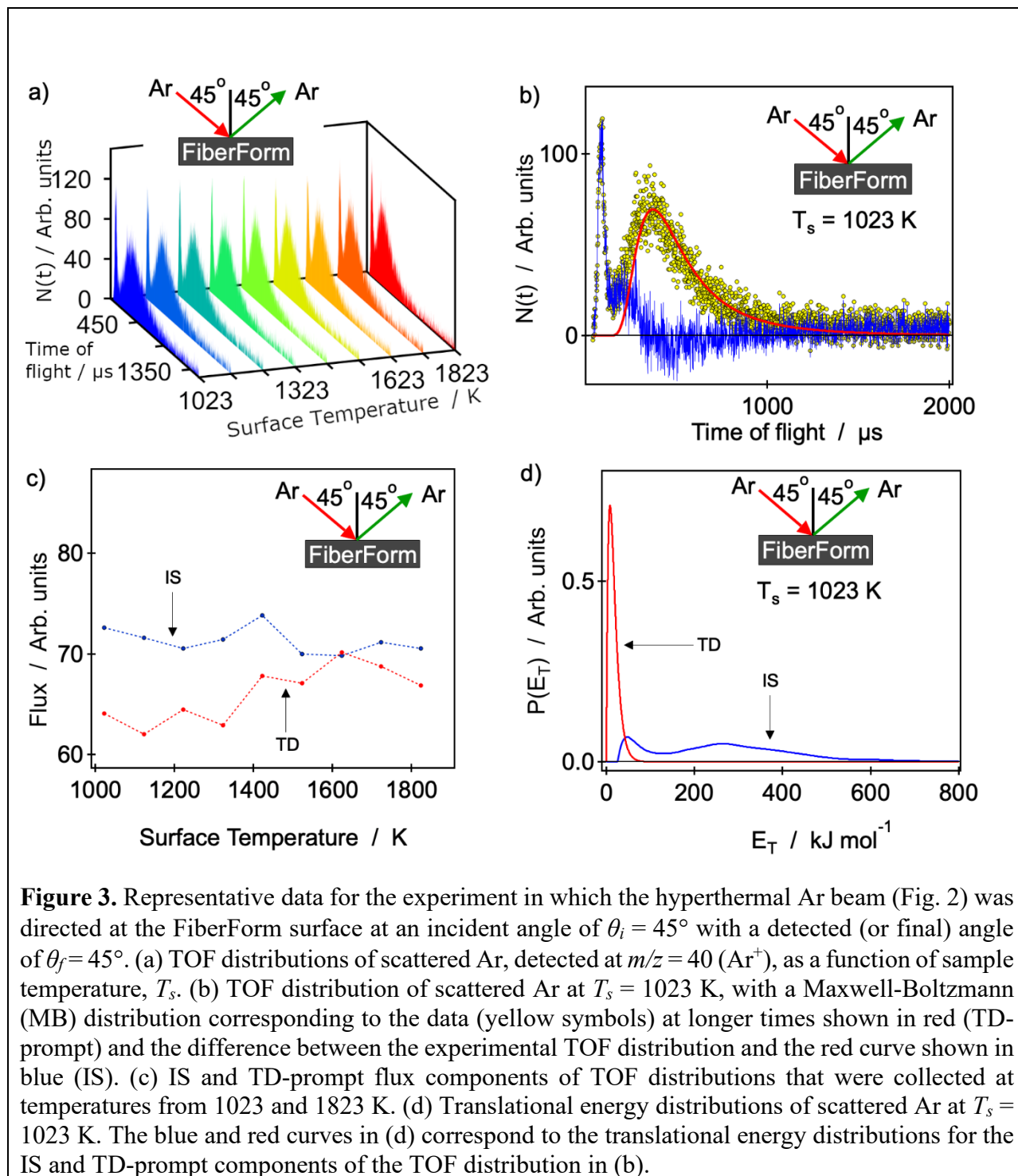


Figure 2. Translational energy distributions of the velocity-selected incident hyperthermal O, O₂, and Ar beams. The blue and red curves represent the O and O₂ distributions, respectively, used during collection of temperature survey data. The green curve represents the distribution for incident Ar. The maximum values of the translational energy distributions for Ar and O have been normalized to 1.0, and the relative areas under the O and O₂ distributions correspond to the mole fractions of these species in the incident O/O₂ beam. The translational energy distributions used for the experiment in which angular distributions were collected are shown in Figure S1.



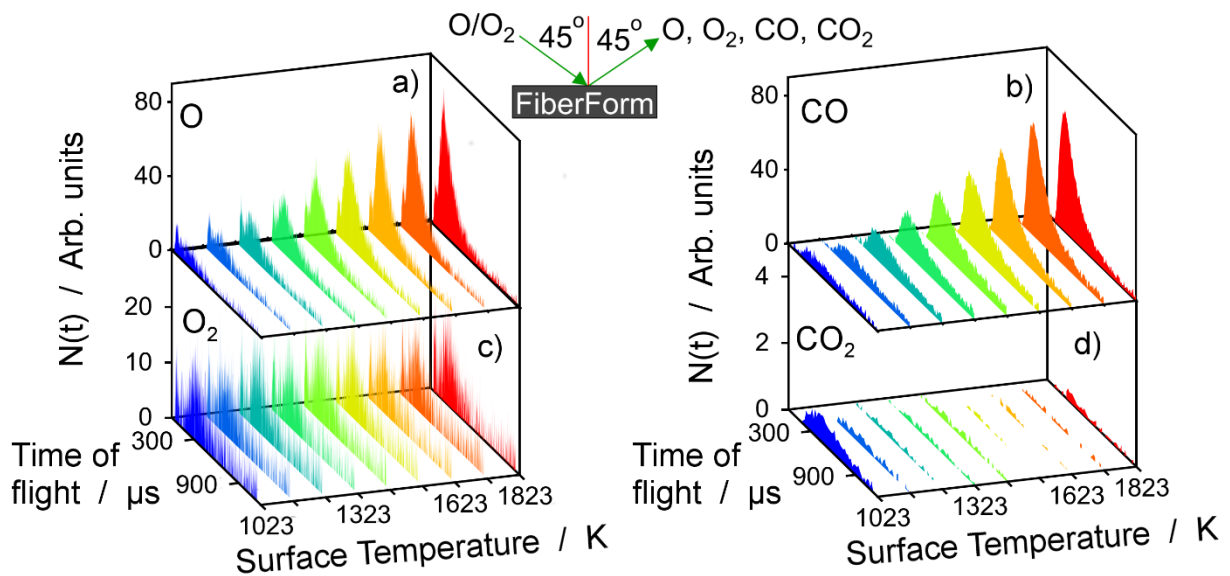


Figure 4. TOF distributions as a function of sample temperature collected with the incident O/O₂ beam (Fig. 2) striking the FiberForm surface, corresponding to $\theta_i = \theta_f = 45^\circ$ for (a) O, detected at $m/z = 16$ (O⁺), (b) CO, detected at $m/z = 28$ (CO⁺), (c) O₂, detected at $m/z = 32$ (O₂⁺), and (d) CO₂ detected at $m/z = 44$ (CO₂⁺).

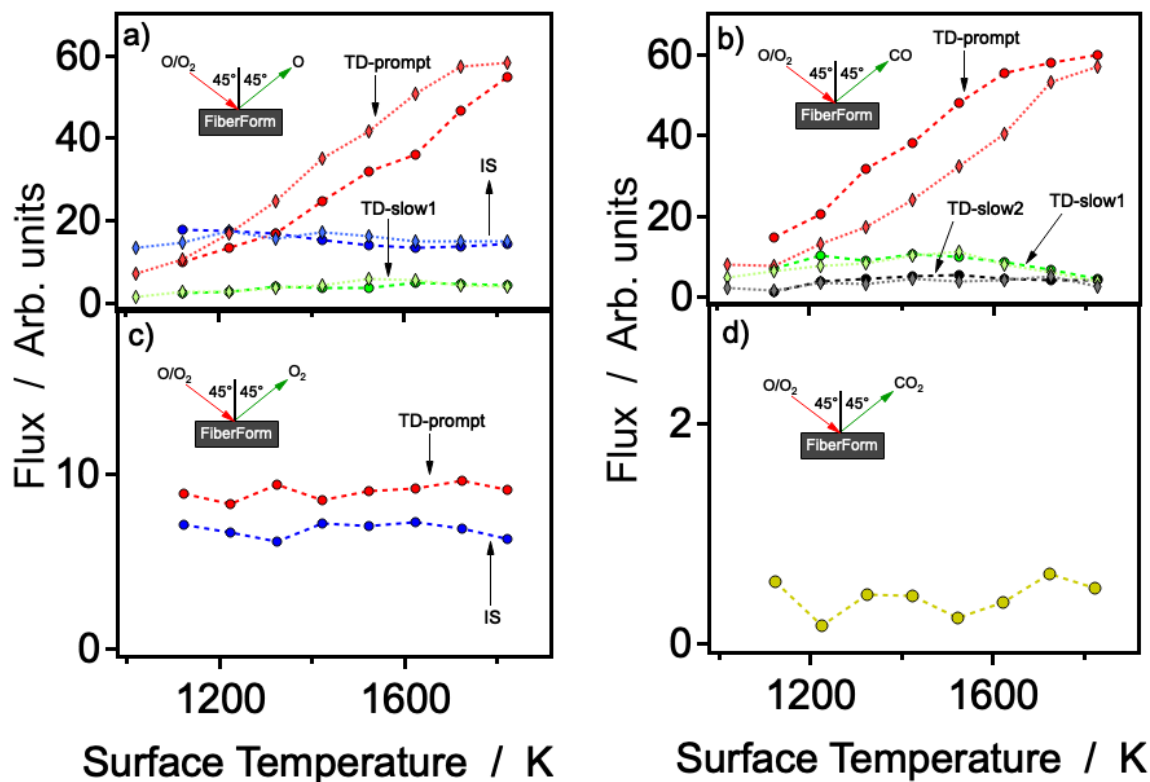


Figure 5. Flux components derived from the data shown in Fig. 4. Blue, red, green, and black represent IS, TD-prompt, TD-slow1, and TD-slow2 components, respectively. The circles represent flux with increasing sample temperature, and diamonds represent flux with decreasing sample temperature. The CO flux in (b) was obtained using the residual fitting method, described in the text. The total flux of CO₂ is shown because the flux of CO₂ was small and meaningful component fluxes could not be obtained. The fluxes have been corrected for the ionization cross-section and the relative number of molecular beam pulses used to accumulate the data; thus, the fluxes of the species collected under different conditions may be compared directly.

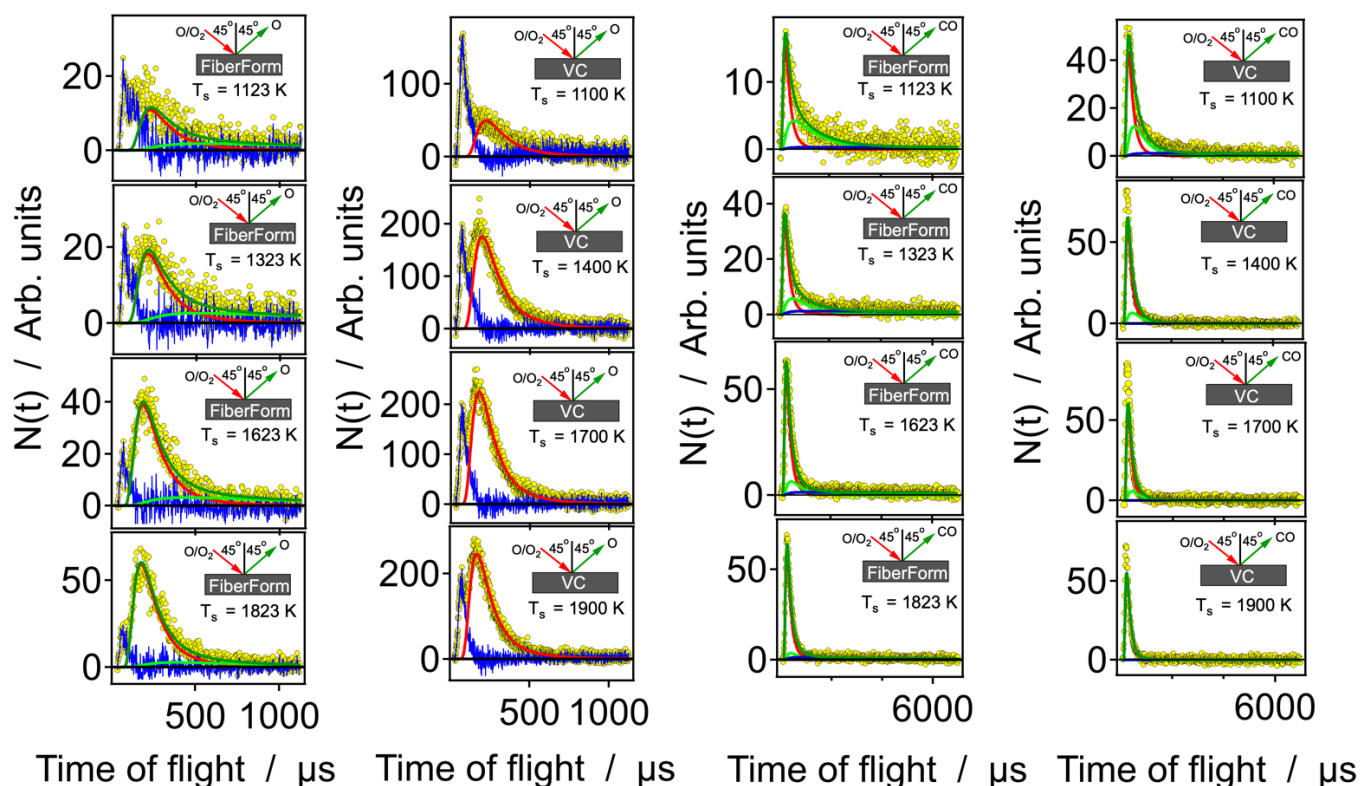


Figure 6. Representative TOF distributions for O (a, b) and CO (c, d), collected for $\theta_i = \theta_f = 45^\circ$ when the hyperthermal O/O₂ beam was incident on FiberForm and vitreous carbon (VC) surfaces at four temperatures, as shown. Yellow, blue, red, light green, and dark green in (a, b) represent total, IS, TD-prompt, TD-slow, and sum of both TD components, respectively. There is no obvious TD-slow component in the TOF distributions of O from vitreous carbon. For (c, d), yellow, red, light green, blue, and dark green represent total, TD-prompt, TD-slow1, TD-slow2, and sum of all TD components, respectively. A small IS component in TOF distributions for CO from vitreous carbon (d) is not shown. The O data (a, b) were analyzed over a 1200 μs range, whereas the CO data were analyzed over a 20,000 μs range. Only the first 7000 μs of the TOF distributions for CO (c, d) are shown. The number densities have been corrected for the ionization cross-section and the relative number of molecular beam pulses used to accumulate the data; thus, the number densities of the two species collected under different conditions may be compared directly.

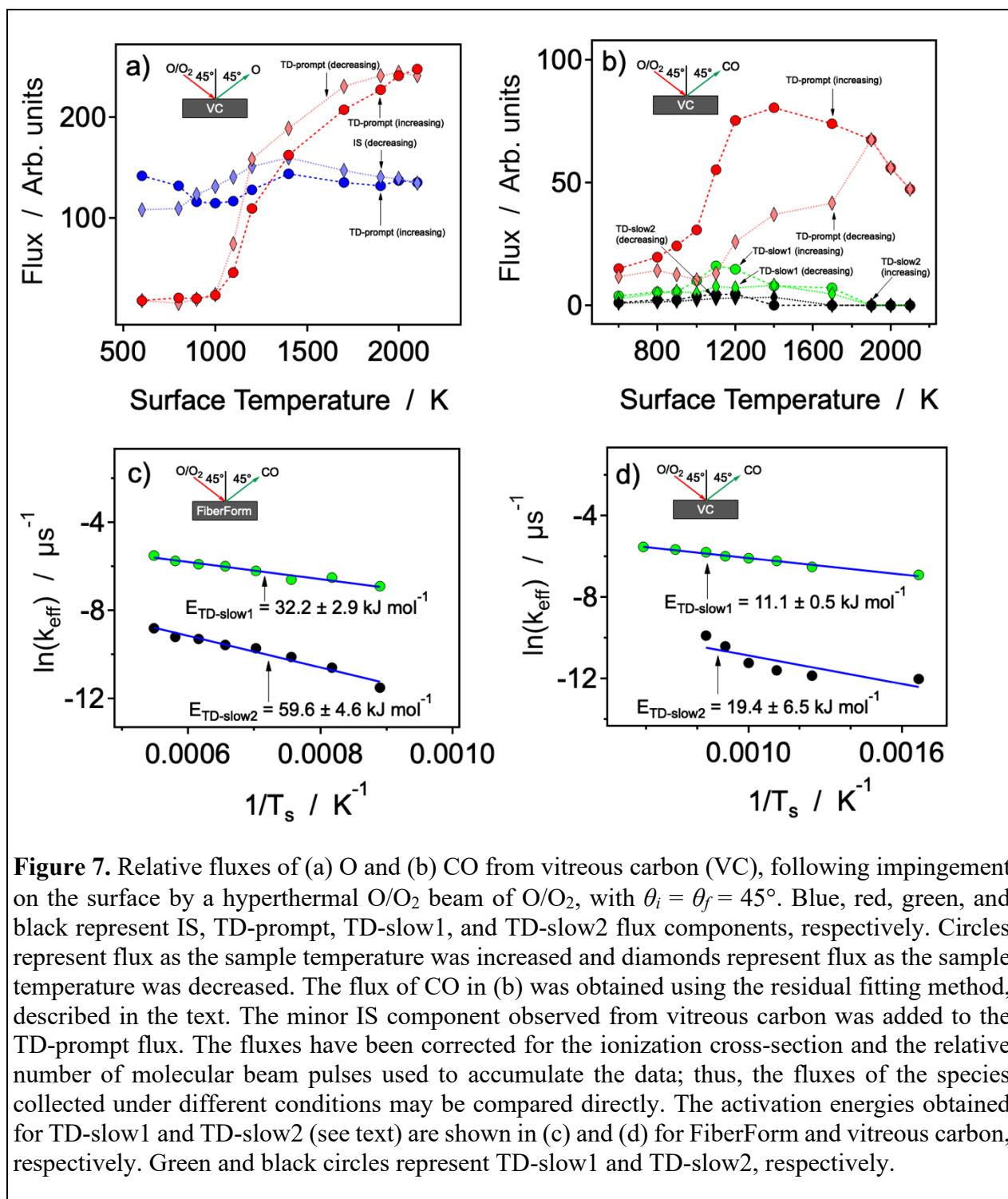


Figure 7. Relative fluxes of (a) O and (b) CO from vitreous carbon (VC), following impingement on the surface by a hyperthermal O/O₂ beam of O/O₂, with $\theta_i = \theta_f = 45^\circ$. Blue, red, green, and black represent IS, TD-prompt, TD-slow1, and TD-slow2 flux components, respectively. Circles represent flux as the sample temperature was increased and diamonds represent flux as the sample temperature was decreased. The flux of CO in (b) was obtained using the residual fitting method, described in the text. The minor IS component observed from vitreous carbon was added to the TD-prompt flux. The fluxes have been corrected for the ionization cross-section and the relative number of molecular beam pulses used to accumulate the data; thus, the fluxes of the species collected under different conditions may be compared directly. The activation energies obtained for TD-slow1 and TD-slow2 (see text) are shown in (c) and (d) for FiberForm and vitreous carbon, respectively. Green and black circles represent TD-slow1 and TD-slow2, respectively.

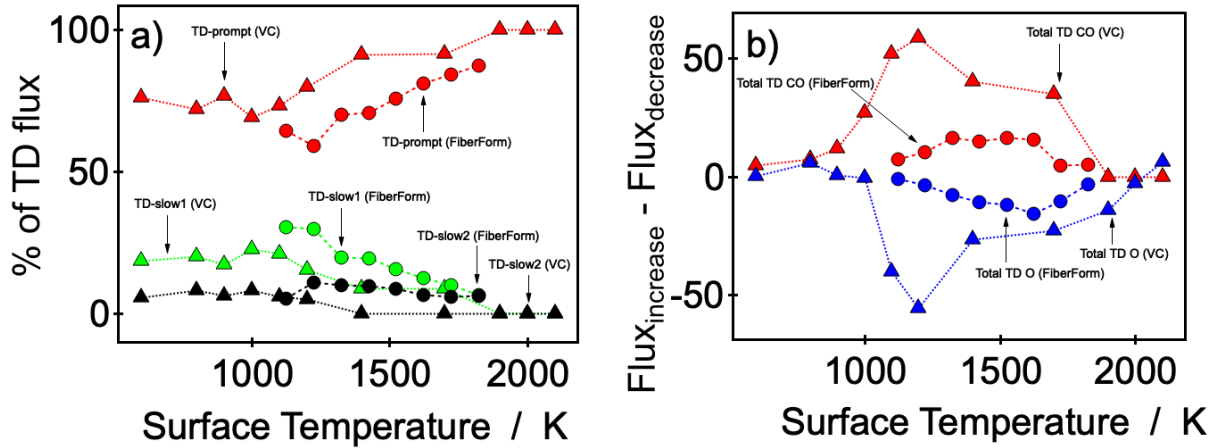


Figure 8. (a) Percentage of TD-prompt, TD-slow1, and TD-slow2 fluxes for reactively scattered CO from FiberForm and vitreous carbon. The percentage is computed as $100 \cdot \text{CO}_i / \text{CO}_{total}$, where i represents prompt or slow flux and $total$ represents the sum of all thermal flux components. Red, green, and black represent TD-prompt, TD-slow1, and TD-slow2 respectively. Circles represent percentages for FiberForm and triangles represent percentages for vitreous carbon. (b) The difference between the curves corresponding to increasing and decreasing temperature in Fig. 7a (O, blue) and Fig. 7b (CO, red). Circles represent flux from FiberForm and triangles represent flux from vitreous carbon. Total TD in (b) represents sum of all thermal fluxes (TD-prompt+TD-slow1+TD-slow2), where TD-slow2 applies only for CO.

References

- [1] M. Mahzari, R.D. Braun, T.R. White, D. Bose, Inverse Estimation of the Mars Science Laboratory Entry Aeroheating and Heatshield Response, *J. Spacecr. Rockets*. 52 (2015) 1203–1216.
- [2] B.K. Bessire, T.K. Minton, Decomposition of phenolic impregnated carbon ablator (PICA) as a function of temperature and heating rate, *ACS Appl. Mater. Interfaces*. 9 (2017) 21422–21437.
- [3] B.K. Bessire, S.A. Lahankar, T.K. Minton, Pyrolysis of phenolic impregnated carbon ablator (PICA), *ACS Appl. Mater. Interfaces*. 7 (2015) 1383–1395.
- [4] F.S. Milos, Y.-K. Chen, Ablation and thermal response property model validation for phenolic impregnated carbon ablator, *J. Spacecr. Rockets*. 47 (2010) 786–805.
- [5] S. Poovathingal, T.E. Schwartzentruber, V.J. Murray, T.K. Minton, G.V. Candler, Finite-rate oxidation model for carbon surfaces from molecular beam experiments, *AIAA J.* (2017) 1644–1658.
- [6] S. Poovathingal, T.E. Schwartzentruber, V.J. Murray, T.K. Minton, Molecular simulation of carbon ablation using beam experiments and resolved microstructure, *AIAA J.* 54 (2016) 999–1010.
- [7] C.R. Alba, R.B. Greendyke, Nonequilibrium finite-rate carbon ablation model for earth reentry flows, *J. Spacecr. Rockets*. (2016) 579–583.
- [8] A. Borner, K. Swaminathan-Gopalan, K. Stephani, V.J. Murray, S. Poovathingal, T.K. Minton, F. Panerai, N.N. Mansour, Detailed DSMC surface chemistry modeling of the oxidation of light-weight carbon preform ablators, in: 47th AIAA Thermophys. Conf. 2017, American Institute of Aeronautics and Astronautics Inc, AIAA, 2017.
- [9] K. Swaminathan Gopalan, A. Borner, K.A. Stephani, V. Murray, S.J. Poovathingal, T. Minton, N.N. Mansour, DSMC analysis of molecular beam experiments for oxidation of carbon based ablators, in: 55th AIAA Aerosp. Sci. Meet., 2017: p. 1845.
- [10] F. Panerai, A. Martin, N.N. Mansour, S.A. Sepka, J. Lachaud, Flow-tube oxidation experiments on the carbon preform of a phenolic-impregnated carbon ablator, *J. Thermophys. Heat Transf.* 28 (2014) 181–190.
- [11] F. Panerai, J.D. White, T.J. Cochell, O.M. Schroeder, N.N. Mansour, M.J. Wright, A. Martin, Experimental measurements of the permeability of fibrous carbon at high-temperature, *Int. J. Heat Mass Transf.* 101 (2016) 267–273.
- [12] F. Panerai, N.N. Mansour, J. Lachaud, A. Martin, Experimental and numerical study of carbon fiber oxidation, (2014).
- [13] E. Stern, *Microscale Modeling of Porous Thermal Protection System Materials*, (2015).
- [14] K.T. Nicholson, T.K. Minton, S.J. Sibener, Spatially anisotropic etching of graphite by hyperthermal atomic oxygen, *J. Phys. Chem. B*. 109 (2005) 8476–8480.
- [15] R. Larciprete, P. Lacovig, S. Gardonio, A. Baraldi, S. Lizzit, Atomic oxygen on graphite: chemical characterization and thermal reduction, *J. Phys. Chem. C*. 116 (2012) 9900–9908.
- [16] A. Bagri, C. Mattevi, M. Acik, Y.J. Chabal, M. Chhowalla, V.B. Shenoy, Structural evolution during the reduction of chemically derived graphene oxide, *Nat. Chem.* 2 (2010) 581–587.
- [17] F. Stevens, L.A. Kolodny, T.P. Beebe, Kinetics of graphite oxidation: monolayer and multilayer etch pits in HOPG studied by STM, *J. Phys. Chem. B*. 102 (1998) 10799–10804.
- [18] R. Larciprete, S. Fabris, T. Sun, P. Lacovig, A. Baraldi, S. Lizzit, Dual path mechanism in the thermal reduction of graphene oxide, *J. Am. Chem. Soc.* 133 (2011) 17315–17321.

- [19] V.J. Murray, E.J. Smoll Jr, T.K. Minton, Dynamics of graphite oxidation at high temperature, *J. Phys. Chem. C*. 122 (2018) 6602–6617.
- [20] S. Poovathingal, T.E. Schwartzentruber, S.G. Srinivasan, A.C. Van Duin, Large scale computational chemistry modeling of the oxidation of highly oriented pyrolytic graphite, *J. Phys. Chem. A*. 117 (2013) 2692–2703.
- [21] S. Goverapet Srinivasan, A.C. van Duin, Molecular-dynamics-based study of the collisions of hyperthermal atomic oxygen with graphene using the ReaxFF reactive force field, *J. Phys. Chem. A*. 115 (2011) 13269–13280.
- [22] T. Sun, S. Fabris, Mechanisms for oxidative unzipping and cutting of graphene, *Nano Lett.* 12 (2012) 17–21.
- [23] T. Sun, S. Fabris, S. Baroni, Surface precursors and reaction mechanisms for the thermal reduction of graphene basal surfaces oxidized by atomic oxygen, *J. Phys. Chem. C*. 115 (2011) 4730–4737.
- [24] V. Moron, L. Martin-Gondre, C. Crespos, P. Larregaray, P. Gamallo, R. Sayós, Classical dynamics study of atomic oxygen over graphite (0 0 0 1) with new interpolated and analytical potential energy surfaces, *Comput. Theor. Chem.* 990 (2012) 132–143.
- [25] H. Kinoshita, M. Umeno, M. Tagawa, N. Ohmae, Hyperthermal atomic oxygen beam-induced etching of HOPG (0001) studied by X-ray photoelectron spectroscopy and scanning tunneling microscopy, *Surf. Sci.* 440 (1999) 49–59.
- [26] K.T. Nicholson, T.K. Minton, S.J. Sibener, Temperature-dependent morphological evolution of HOPG graphite upon exposure to hyperthermal O (3P) atoms, *Prog. Org. Coat.* 47 (2003) 443–447.
- [27] V.J. Murray, B.C. Marshall, P.J. Woodburn, T.K. Minton, Inelastic and reactive scattering dynamics of hyperthermal O and O₂ on hot vitreous carbon surfaces, *J. Phys. Chem. C*. 119 (2015) 14780–14796.
- [28] V.J. Murray, P. Recio, A. Caracciolo, C. Miossec, N. Balucani, P. Casavecchia, T.K. Minton, Oxidation and nitridation of vitreous carbon at high temperatures, *Carbon*. 167 (2020) 388–402.
- [29] J.R. Walls, R.F. Strickland-Constable, Oxidation of carbon between 1000–2400 C, *Carbon*. 1 (1964) 333–338.
- [30] H.D. Allendorf, D.E. Rosner, Primary products in the attack of graphite by atomic oxygen and diatomic oxygen above 1100 K, *Carbon*. 7 (1969) 515–518.
- [31] K.A. Trumble, I. Cozmuta, S. Sepka, P. Jenniskens, M. Winter, Postflight aerothermal analysis of the stardust sample return capsule, *J. Spacecr. Rockets*. 47 (2010) 765–774.
- [32] R.P. Kornfeld, R. Prakash, A.S. Devereaux, M.E. Greco, C.C. Harmon, D.M. Kipp, Verification and validation of the Mars Science Laboratory/Curiosity rover entry, descent, and landing system, *J. Spacecr. Rockets*. 51 (2014) 1251–1269.
- [33] R.A. Beck, D.M. Driver, M.J. Wright, H.H. Hwang, K.T. Edquist, S.A. Sepka, Development of the mars science laboratory heatshield thermal protection system, *J. Spacecr. Rockets*. 51 (2014) 1139–1150.
- [34] H. Tran, C. Johnson, D. Rasky, F. Hui, M.-T. Hsu, Y. Chen, Phenolic impregnated carbon ablaters (PICA) for Discovery Class missions, in: 31st Thermophys. Conf., 1996: p. 1911.
- [35] E. Musk, COTS Status Update & Crew Capabilities, (2009) 37.
- [36] K. Fujita, T. Suzuki, S. Matsuyama, T. Yamada, S. Abe, Numerical Reconstruction of HAYABUSA Sample Return Capsule Flight Environments, in: 42nd AIAA Thermophys. Conf., 2011: p. 3477.

- [37] S. Loehle, T. Hermann, F. Zander, Experimental assessment of the performance of ablative heat shield materials from plasma wind tunnel testing, *CEAS Space J.* 10 (2018) 203–211.
- [38] FiberMaterials Inc., FiberForm precursor, (n.d.).
- [39] D.J. Garton, A.L. Brunsvold, T.K. Minton, D. Troya, B. Maiti, G.C. Schatz, Experimental and theoretical investigations of the inelastic and reactive scattering dynamics of O (3 P)+ D₂, *J. Phys. Chem. A.* 110 (2006) 1327–1341.
- [40] A.L. Brunsvold, H.P. Upadhyaya, J. Zhang, R. Cooper, T.K. Minton, M. Braunstein, J.W. Duff, Dynamics of Hyperthermal Collisions of O (3P) with CO, *J. Phys. Chem. A.* 112 (2008) 2192–2205.
- [41] J. Zhang, D.J. Garton, T.K. Minton, Reactive and inelastic scattering dynamics of hyperthermal oxygen atoms on a saturated hydrocarbon surface, *J. Chem. Phys.* 117 (2002) 6239–6251.
- [42] J. Zhang, H.P. Upadhyaya, A.L. Brunsvold, T.K. Minton, Hyperthermal Reactions of O and O₂ with a Hydrocarbon Surface: Direct C–C Bond Breakage by O and H-Atom Abstraction by O₂, *J. Phys. Chem. B.* 110 (2006) 12500–12511.
- [43] G.E. Caledonia, R.H. Krech, B.D. Green, A high flux source of energetic oxygen atoms for material degradation studies, *AIAA J.* 25 (1987) 59–63.
- [44] D.J. Garton, T.K. Minton, B. Maiti, D. Troya, G.C. Schatz, A crossed molecular beams study of the O (3 P)+ H₂ reaction: comparison of excitation function with accurate quantum reactive scattering calculations, *J. Chem. Phys.* 118 (2003) 1585–1588.
- [45] D. Troya, G.C. Schatz, D.J. Garton, A.L. Brunsvold, T.K. Minton, Crossed beams and theoretical studies of the O (3 P)+ CH₄→ H+ OCH₃ reaction excitation function, *J. Chem. Phys.* 120 (2004) 731–739.
- [46] G.O. Brink, Electron bombardment molecular beam detector, *Rev. Sci. Instrum.* 37 (1966) 857–860.
- [47] N.R. Daly, Scintillation type mass spectrometer ion detector, *Rev. Sci. Instrum.* 31 (1960) 264–267.
- [48] B.C. Marshall, E.J. Smoll Jr, S.M. Purcell, M.L. Costen, K.G. McKendrick, T.K. Minton, Scattering dynamics of oxygen atoms on imidazolium tetrafluoroborate ionic liquid surfaces: Dependence on alkyl chain length, *J. Phys. Chem. C.* 120 (2016) 12472–12483.
- [49] D.J. Garton, T.K. Minton, M. Alagia, N. Balucani, P. Casavecchia, G.G. Volpi, Reactive scattering of ground-state and electronically excited oxygen atoms on a liquid hydrocarbon surface, *Faraday Discuss.* 108 (1997) 387–399.
- [50] B. Wu, J. Zhang, T.K. Minton, K.G. McKendrick, J.M. Slattery, S. Yockel, G.C. Schatz, Scattering dynamics of hyperthermal oxygen atoms on ionic liquid surfaces:[emim][NTf₂] and [C12mim][NTf₂], *J. Phys. Chem. C.* 114 (2010) 4015–4027.
- [51] W.A. Alexander, J. Zhang, V.J. Murray, G.M. Nathanson, T.K. Minton, Kinematics and dynamics of atomic-beam scattering on liquid and self-assembled monolayer surfaces, *Faraday Discuss.* 157 (2012) 355–374.
- [52] M.E. King, M.E. Saecker, G.M. Nathanson, The thermal roughening of liquid surfaces and its effect on gas–liquid collisions, *J. Chem. Phys.* 101 (1994) 2539–2547.
- [53] M.E. Saecker, S.T. Govoni, D.V. Kowalski, M.E. King, G.M. Nathanson, Molecular beam scattering from liquid surfaces, *Science.* 252 (1991) 1421–1424.
- [54] K.P. Giapis, T.A. Moore, T.K. Minton, Hyperthermal neutral beam etching, *J. Vac. Sci. Technol. Vac. Surf. Films.* 13 (1995) 959–965.

- [55] T.K. Minton, K.P. Giapis, T. Moore, Inelastic scattering dynamics of hyperthermal fluorine atoms on a fluorinated silicon surface, *J. Phys. Chem. A.* 101 (1997) 6549–6555.
- [56] E.J. Smoll Jr, T.K. Minton, Scattering-Angle Randomization in Nonthermal Gas–Liquid Collisions, *J. Phys. Chem. C.* 123 (2019) 22887–22896.
- [57] M.E. King, G.M. Nathanson, M. Hanning-Lee, T.K. Minton, Probing the microscopic corrugation of liquid surfaces with gas-liquid collisions, *Phys. Rev. Lett.* 70 (1993) 1026.
- [58] D.R. Olander, W. Siekhaus, R. Jones, J.A. Schwarz, Reactions of modulated molecular beams with pyrolytic graphite. I. Oxidation of the basal plane, *J. Chem. Phys.* 57 (1972) 408–420.
- [59] K.D. Gibson, S.J. Sibener, H.P. Upadhyaya, A.L. Brunsvold, J. Zhang, T.K. Minton, D. Troya, Hyperthermal Ar atom scattering from a C (0001) surface, *J. Chem. Phys.* 128 (2008) 224708.
- [60] B. Marchon, W.T. Tysoe, J. Carrazza, H. Heinemann, G.A. Somorjai, Reactive and kinetic properties of carbon monoxide and carbon dioxide on a graphite surface, *J. Phys. Chem.* 92 (1988) 5744–5749.
- [61] J. Hunt, A. Ferrari, A. Lita, M. Crosswhite, B. Ashley, A.E. Stiegman, Microwave-specific enhancement of the carbon–carbon dioxide (Boudouard) reaction, *J. Phys. Chem. C.* 117 (2013) 26871–26880.
- [62] P.L. Walker Jr, F. Rusinko Jr, L.G. Austin, Gas reactions of carbon, in: *Adv. Catal.*, Elsevier, 1959: pp. 133–221.
- [63] S. Ergun, Kinetics of the reaction of carbon with carbon dioxide, *J. Phys. Chem.* 60 (1956) 480–485.
- [64] P.C. Koenig, R.G. Squires, N.M. Laurendeau, Evidence for two-site model of char gasification by carbon dioxide, *Carbon.* 23 (1985) 531–536.
- [65] A.A. Lizzio, H. Jiang, L.R. Radovic, On the kinetics of carbon (char) gasification: reconciling models with experiments, *Carbon.* 28 (1990) 7–19.
- [66] G. Tremblay, F.J. Vastola, P.L. Walker Jr, Thermal desorption analysis of oxygen surface complexes on carbon, *Carbon.* 16 (1978) 35–39.
- [67] J.L. Figueiredo, M.F.R. Pereira, M.M.A. Freitas, J.J.M. Orfao, Modification of the surface chemistry of activated carbons, *Carbon.* 37 (1999) 1379–1389.
- [68] J.-H. Zhou, Z.-J. Sui, J. Zhu, P. Li, D. Chen, Y.-C. Dai, W.-K. Yuan, Characterization of surface oxygen complexes on carbon nanofibers by TPD, XPS and FT-IR, *Carbon.* 45 (2007) 785–796.
- [69] A. Bagri, R. Grantab, N.V. Medhekar, V.B. Shenoy, Stability and formation mechanisms of carbonyl- and hydroxyl-decorated holes in graphene oxide, *J. Phys. Chem. C.* 114 (2010) 12053–12061.
- [70] J.M. Carlsson, F. Hanke, S. Linic, M. Scheffler, Two-step mechanism for low-temperature oxidation of vacancies in graphene, *Phys. Rev. Lett.* 102 (2009) 166104.
- [71] J.T. Paci, I. Paci, Theoretical Studies of the Reactions between Hyperthermal O (3P) and Graphite: Holes and the Second Layer, *J. Phys. Chem. C.* 123 (2019) 29647–29655.
- [72] Y. Wang, R. Nieman, T.K. Minton, H. Guo, Insights into adsorption, diffusion, and reactions of atomic nitrogen on a highly oriented pyrolytic graphite surface, *J. Chem. Phys.* 154 (2021) 074708.
- [73] D.R. Olander, W. Siekhaus, R. Jones, J.A. Schwarz, Reactions of modulated molecular beams with pyrolytic graphite. I. Oxidation of the basal plane, *J. Chem. Phys.* 57 (1972) 408–420.

- [74] J.A. Britten, J.L. Falconer, L.F. Brown, Effect of nonreacting gases on the desorption of reaction-created CO from graphite, *Carbon*. 23 (1985) 627–633.
- [75] P.L. Walker Jr, L. Pentz, D.L. Biederman, F.J. Vastola, The influence of “inert” diluent gases on the rate of carbon gasification, *Carbon*. 15 (1977) 165–168.

Supporting Information

for

Reactive and Inelastic Scattering Dynamics of Hyperthermal O and O₂ from a Carbon Fiber Network

Savio J. Poovathingal,^{1,*} Min Qian,² Vanessa J. Murray,³ and Timothy K. Minton^{4,*}

¹*Department of Mechanical Engineering, 151 Ralph G. Anderson Building, Lexington, KY 40506, USA; saviopoovathingal@uky.edu; ORCID 0000-0001-7350-5104*

²*Department of Physics, School of Science, East China University of Science and Technology, Shanghai, 200237, China; mqian@ecust.edu.cn; ORCID 0000-0002-6472-7693*

³*Air Force Research Laboratory, Space Vehicles Directorate, 3550 Aberdeen Ave. SE, Kirtland AFB, NM 87117, USA; vanessa.j.murray@gmail.com*

⁴*Ann and H.J. Smead Department of Aerospace Engineering Sciences, 3775 Discovery Dr., University of Colorado Boulder, Boulder, CO 80303, USA; tminton@colorado.edu; ORCID 0000-0003-4577-7879*

*Corresponding Author. Tel: 859 562-2854. E-mail: saviopoovathingal@uky.edu (Savio J. Poovathingal)

*Corresponding Author. Tel: 406 581-1080. E-mail: tminton@colorado.edu (Timothy K. Minton)

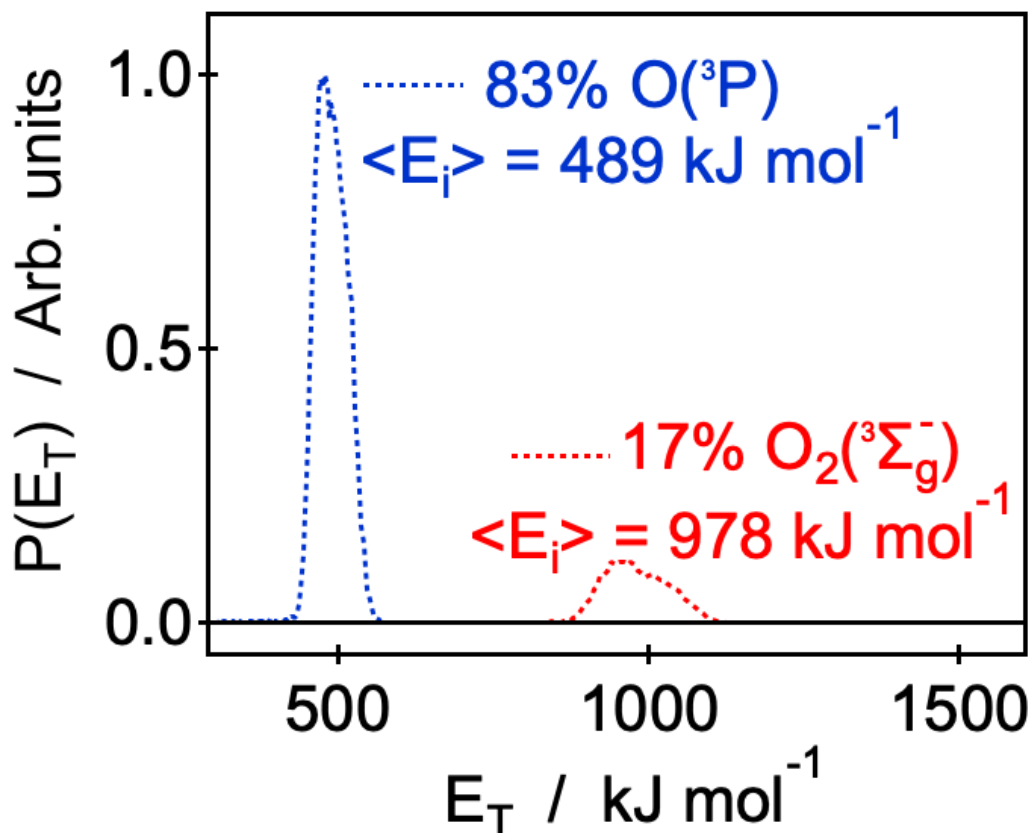


Figure S1. Translational energy distributions of incident O and O₂ for the experiment in which angular distributions were collected. Blue represents the energy distribution of O, and red represents the energy distribution of O₂. The maximum value of the energy distribution for O has been normalized to 1.0, and the relative areas under the curves correspond to the mole fractions of O and O₂ in the incident beam.

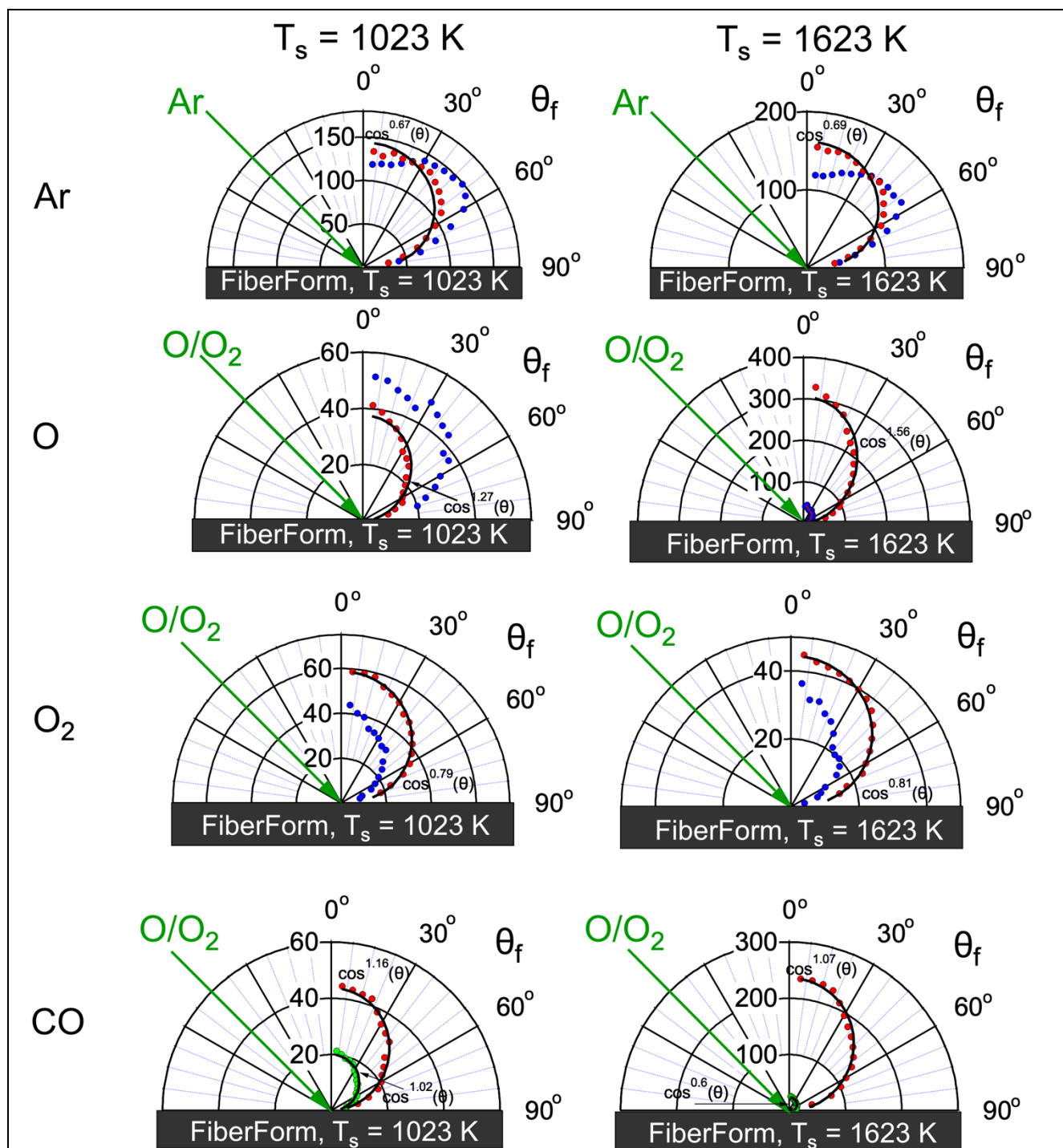
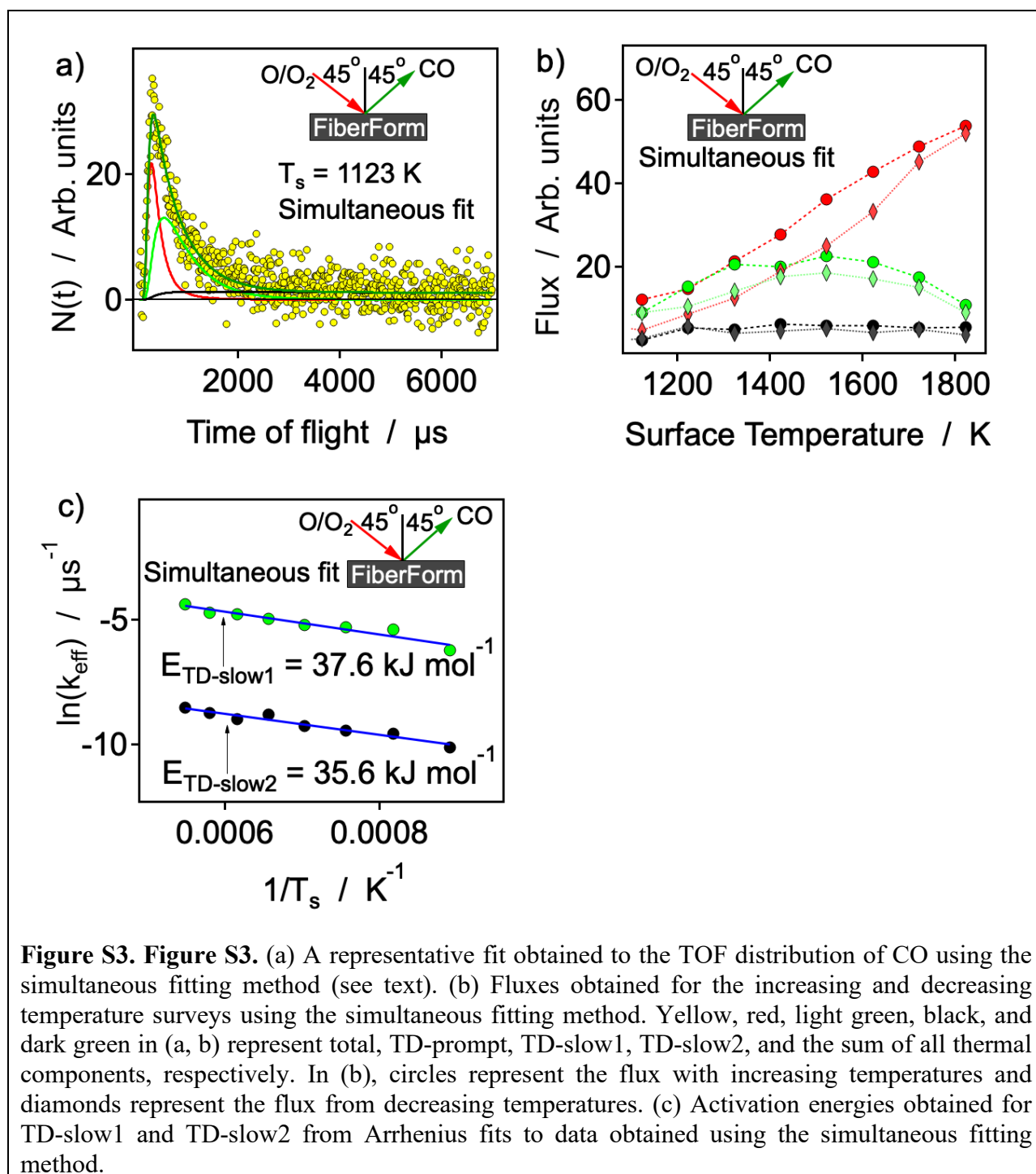
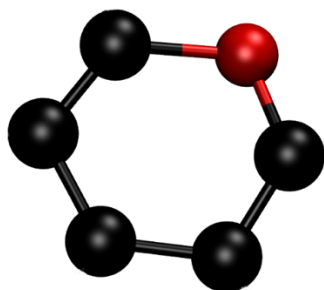


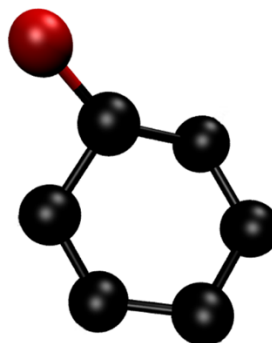
Figure S2. Angular distributions of scattered products, collected with a sample temperatures of $T_s = 1023$ K (left) and 1623 K (right). Blue and red symbols indicate IS and TD-prompt components, respectively, while the green symbols indicate the TD-slow component. The TD component in each case is fit with a cosine-power distribution (black solid lines). The cosine-power law corresponding to TD-prompt and TD-slow is shown in each figure. The angular distributions of TD-slow1 for O and TD-slow2 for CO are not shown here, because the signals were small relative to the other thermal components.



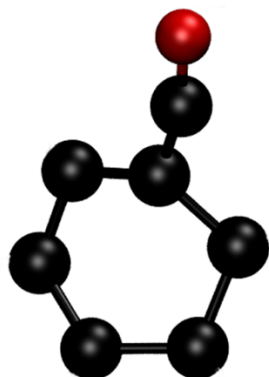
a) Ether



b) Semi-quinone



c) Carbonyl



d) Ether-lactone pair

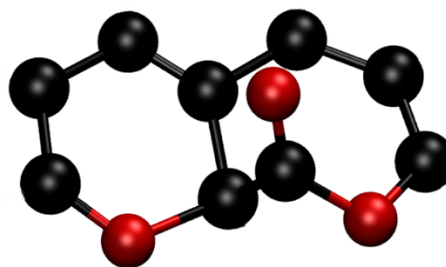


Figure S4. Representative carbon-oxygen functional groups.

1. Correcting observed temperature from pyrometer measurements

Because we use the surface temperature to obtain the TD-prompt component of the experimental data, we evaluate the influence of potential errors arising from measuring surface temperature using an optical pyrometer. Optical pyrometers are calibrated for a black body, and the observed temperature is usually corrected using Wein's displacement law (Branstetter, J. R. *Some practical aspects of surface temperature measurement by optical and ratio pyrometers*. NASA TN D-3604; NASA, Washington, DC, USA, 1966). The equation for correcting the observed temperature is

$$\frac{1}{T_c} - \frac{1}{T_o} = \frac{\lambda \cdot 10^{-8}}{c_2} \ln \varepsilon$$

In the equation above, T_c is the corrected temperature, T_o is the temperature observed from the pyrometer, λ is the optical wavelength in Angstroms, $c_2 = 1.348$, and ε is the emissivity. The difference between the observed and corrected temperatures increases with longer wavelengths and lower emissivity. The emissivity of a carbon surface is usually greater than 0.8 and an oxidized carbon surface would have a higher emissivity (Seo, S.-K.; Roh, J.-S.; Kim, E.-S.; Chi, S.-H.; Kim, S. H.; Lee, S. W. Thermal emissivity of a nuclear graphite as a function of its oxidation degree (2)-effect of surface structural changes. *Carbon Lett.* **2009**, *10*, 300–304). The optical wavelength used for measurements with the pyrometer is in the vicinity of 0.65 μm . We evaluate the corrected temperature (T_c) at 0.65 μm and at a much higher wavelength of 1.3 μm to illustrate the error that could be introduced in the surface temperature measurements.

The difference between T_c and T_o is shown in Figure S5 for $\varepsilon = 0.8$ and two optical wavelengths. The maximum difference in temperature is less than 5% at 1823 K. The corrected temperatures ($T_c = 1857$ and 1892 K) at the two optical wavelengths are used to compute the

thermal flux components of CO recorded at $T_o = 1823$ K and the percentage difference is shown in Table S1. The differences in the flux components are less than 5%. We emphasize here that the errors are likely to be much lower than 5%, as the estimates we used are highly conservative. The error decreases with shorter wavelengths and higher emissivity. Therefore, the errors in surface temperature and the TD flux are expected to be much lower. Hence, we chose not to apply the temperature correction and use the observed temperature from the pyrometer for our analysis.

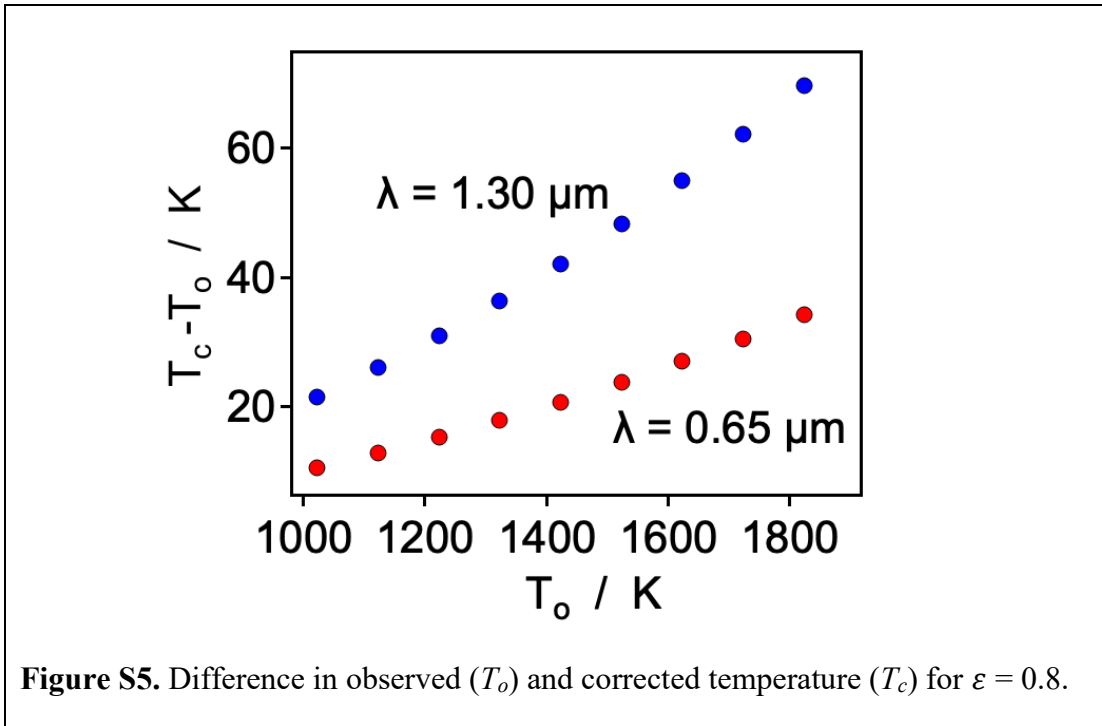


Table S1. The difference in thermal flux components of CO scattered from FiberForm obtained using $T_c = 1857$ K and 1892 K. The difference is computed as a percentage of flux obtained as $100 * |\text{Flux}_{T_c} - \text{Flux}_{T_o}| / \text{Flux}_{T_o}$.

T_c	TD-prompt	TD-slow1	TD-slow2
1857	1.9	1.3	0.5
1893	4.4	3.8	0.8

2. Resolution of time-of-flight distributions

To estimate the time resolution of a time-of-flight (TOF distribution), a time window was chosen to perform the analysis. The lower bound of the window was chosen as $t_{min} = \frac{d}{2} \sqrt{\frac{m}{RT}}$ and the upper bound (t_{max}) is chosen such that 75% of the flux is accounted for. The TD-prompt fit is most sensitive to this region of the data. In the time window that we chose, we assumed that the signals arose purely from a TD-prompt process. The noise in the TOF distributions can be estimated by computing the absolute difference between the Maxwell-Boltzmann fit and the experimental signal. The noise as a function of channel is shown in Figure S6a for three different surface temperatures. The TOF distributions obtained from the experiment and the Maxwell-Boltzmann fit for Ar at $T_s = 1023$ K are shown in Figure S6b, where yellow symbols represent the experimental data and the red curve represents the Maxwell-Boltzmann fit (TD-prompt). An average noise is computed over the time window, and a pseudo signal (green curve in Figure S6b) is generated by adding the average noise to the TD-prompt fit. The true signal (depicted by the red curve in Figure S6b) captures any thermal event occurring with time scales that are within the green curve. Therefore, thermal events that are slow and occur at timescales that are outside the range of the green curve would be resolved in our TOF distributions. The time resolution is computed by estimating the time required to translate the true fit (red curve in Figure S6b) outside the green bounds. As a conservative estimate, we choose the magnitude of the upper bound of the time window as the anchor point for translation. The translated curve is shown (blue curve) in Figure S6b, and the translation was $89 \mu\text{s}$ at $T_s = 1023$ K. Thus, thermal events at $T_s = 1023$ K occurring at least $89 \mu\text{s}$ apart would be resolved in the TOF distributions. The analysis described above cannot be performed on the TOF distributions of CO and O at $T_s = 1023$ K, because multiple

thermal events are indistinguishable within the signal-to-noise. However, the analysis can be performed on CO and O at $T_s = 1823$ K because the slow thermal signals are negligible. The time resolutions obtained for CO and O at $T_s = 1823$ K are $12 \mu\text{s}$ and $39 \mu\text{s}$, respectively. The time resolutions at different surface temperatures were similar for Ar, as the thermal flux of scattered Ar was similar in the range of surface temperature investigated. However, the thermal flux of O and CO is much higher at $T_s = 1823$ K compared to the thermal flux at $T_s = 1023$ K. To estimate the time resolution in the TOF distributions of O and CO, we assume that the gradient of the thermal flux and the time resolution as a function of surface temperature are equal. Using this assumption, the time resolutions for CO and O at $T_s = 1023$ K is $112 \mu\text{s}$ and $90 \mu\text{s}$, respectively. As a conservative estimate, slow processes in our experiments would refer to thermal events occurring at time scales greater than $112 \mu\text{s}$.

